Nature
April 2024, Volume 628, Issue 8009, Pages 782-787
https://doi.org/10.1038/s41586-024-07247-w https://archimer.ifremer.fr/doc/00887/99856/

Mid-ocean ridge unfaulting revealed by magmatic intrusions

Olive Jean-Arthur [1,*], Ekström Göran [2], Buck W. Roger [2], Liu Zhonglan [3], Escartín Javier [1], Bickert Manon [4]

[1] Laboratoire de Géologie, CNRS - École Normale Supérieure - PSL University, Paris, France
[2] Lamont-Doherty Earth Observatory, Columbia University, Palisades, NY, USA
[3] College of Earth Sciences, Jilin University, Changchun, China
[4] Geo-Ocean, Univ. Brest, CNRS, Ifremer, UMR6538, Plouzané, France

* Corresponding author : Jean-Arthur Olive, email address : olive@geologie.ens.fr

Abstract :

Mid-ocean ridges (MORs) are quintessential sites of tectonic extension1,2,3,4, at which divergence between lithospheric plates shapes abyssal hills that cover about two-thirds of the Earth's surface5,6. Here we show that tectonic extension at the ridge axis can be partially undone by tectonic shortening across the ridge flanks. This process is evidenced by recent sequences of reverse-faulting earthquakes about 15 km off-axis at the Mid-Atlantic Ridge and Carlsberg Ridge. Using mechanical models, we show that shallow compression of the ridge flanks up to the brittle failure point is a natural consequence of lithosphere unbending away from the axial relief. Intrusion of magma-filled fractures, which manifests as migrating swarms of extensional seismicity along the ridge axis, can provide the small increment of compressive stress that triggers reverse-faulting earthquakes. Through bathymetric analyses, we further find that reverse reactivation of MOR normal faults is a widely occurring process that can reduce the amplitude of abyssal hills by as much as 50%, shortly after they form at the ridge axis. This 'unfaulting' mechanism exerts a first-order influence on the fabric of the global ocean floor and provides a physical explanation for reverse-faulting earthquakes in an extensional environment.

Normal faults are major contributors to the seismic activity of mid-ocean ridges[1–4] (MORs). Over 100s of kyrs, these faults offset and tilt newly accreted volcanic seafloor, shaping regularly spaced abyssal hills[5–7]. Remarkably, normal faults with the largest offsets are typically found on the edges of axial valleys, but almost never in the outer ridge flanks (Fig. 1). This observation, made in the 1970s before multibeam bathymetric data became widely available, led several authors to formulate the concept of abyssal hill unfaulting, i.e., the notion that MOR normal faults experience reverse slip that shortens their offsets as they migrate up the ridge flanks[8–11]. This idea lost favor because no clear driving mechanism had been identified and, most notably, because reverse-faulting earthquakes compatible with ridge-normal compression near the axis had not been reported[12]. Reverse-faulting events are well documented hundreds of km from MOR axes[13], in oceanic lithosphere older than 10–20 Ma, where a compressive stress state is expected[14]. Rare reverse-faulting events have also been observed in lithosphere as young as 3 Ma (~30 km from the axis at slow spreading rates[13]), or even closer to the axis in the vicinity of transform faults[15]. Surprisingly, these events indicate both ridge-parallel and ridge-normal compression (Extended Data Fig. 1a), and have been attributed to either thermal stresses[16], the complex stress state of ridge-transform intersections[17], or recent shifts in plate motion[18]. Clear manifestations of near-axis (< 30 km) compressive seismicity have overall remained elusive, until late 2022.

Swarms of reverse-faulting earthquakes

On September 26th, 2022, a particularly active swarm of earthquakes with moment magnitudes Mw > 4 began at 54ºN on the Northern Mid-Atlantic Ridge[19, 20] (Fig. 1a). This slow-spreading segment (2.2 cm/yr of full plate separation rate) is located north of the Charlie-Gibbs Fracture Zone, and bounded by two non-transform offsets. Its symmetric morphology is typical of a magmatically-robust ridge section (in the sense of ref. 21), with a ~1.3 km deep axial valley flanked by two shoulders, and abyssal hill bounding normal faults with a characteristic spacing of 2–4 km (Fig. 1c). During the first 3 days of the 2022 swarm, relocated seismicity (Methods, Supplementary Table 1) showed southward migration along the axial valley by ~45 km (Extended Data Fig. 2a), and entirely consisted of E-W extensional mechanisms. This normal-faulting activity continued for 27 more days without clear signs of further migration. 80 hours into the swarm, a magnitude-5.1 reverse-faulting earthquake indicative of ridge-normal compression occurred below the summit of the ridge shoulder, 15 km east of the neovolcanic axis. Between September 29, 2022 and January 4, 2023, 11 more reverse-faulting events with Mw up to 5.9 occurred on N-S striking, ~45–50º-dipping planes, outlining two narrow bands symmetrically located ~15 km east and west of the ridge axis (Fig. 1a). Inspection of the teleseismic P waveforms from the largest compressive events shows a very short delay between the direct P arrival and phases reflected off the seafloor and sea surface. This implies remarkably shallow hypocenter depths, which we estimate within 2–5 km below seafloor (Methods).

We identified a similar pattern in a November 2014 earthquake sequence on the slow-spreading Carlsberg Ridge at 6ºN in the Indian Ocean (full spreading rate: 2.4 cm/yr; Fig. 1b, d). There, a less active swarm of Mw~5 normal-faulting seismicity at the ridge axis (with possible, though unclear, southeastward migration: Extended Data Fig. 2e–h) preceded 5 reverse-faulting events ~15 km NE and SW of the ridge axis. Interestingly, both ridge flanks had produced similar Mw 5–5.3 reverse-faulting events in 2005 and 2009 that were not preceded by a detectable swarm of normal-faulting earthquakes.

Compression of mid-ocean ridge flanks

Sparse bathymetric data shows that the 6ºN segment of the Carlsberg Ridge is morphologically similar to the 54ºN segment of the Mid-Atlantic Ridge, with even more pronounced axial relief (Fig. 1c, d). By summing the offsets of major normal faults on both sides of the axis[22–24] (Methods), we estimate the tectonically-accommodated fraction of plate separation T at ~15% in both segments (Fig. 2). The remaining ~85% of plate divergence occurs through magmatic emplacement and could be achieved by, for example, the intrusion of a meter-wide dike through the axial lithosphere every ~50 years[25, 26]. Such partitioning of magmatic and tectonic strain likely explains the formation of regularly-spaced abyssal hills bounded by faults that accumulate normal offsets as large as ~500 m when they grow along the edges of the axial valley[7, 27, 28]. The geometry of the compressive events detected in both segments however indicates that the shallow portion of these normal faults can be reactivated in a reverse sense once they migrate out of the axial valley and reach the top of the ridge shoulders.

Standard numerical simulations of MORs show that the formation of an axial valley results in compressional faulting on the ridge flanks, even when dike intrusion accounts for most of the plate spreading (Fig. 3a). Here we model an idealized 2-D cross-axis section of a slow-spreading center where a fraction M (= 1 - T) of the far-field extension ($2U$) is accommodated by continuous magmatic emplacement in a narrow axial zone[27–29]. In this simulation, the value of M is a self-evolving function of the axial relief, which accounts for mechanical feedbacks between relief development and dike intrusions in the axial zone[30, 31] (Methods). M is adjusted to yield a characteristic abyssal-hill spacing of ~3 km following ref. 7. The development of shoulders is a natural consequence of the vertical displacement that accompanies tectonic extension at the ridge axis: as it moves off axis, uplifted lithosphere must unbend to transition to a state of rigid horizontal motion[32]. This occurs over a characteristic flexural length scale α modulated by the integrated strength of young oceanic lithosphere. In the simulation shown in Fig. 3a, the thermal structure of the ridge is fixed, and chosen such that the visco-elasto-plastic lithosphere flexes into shoulders similar to those of the 54ºN segment of the Mid-Atlantic Ridge. This produces a zone of shallow horizontal compression ~25 km wide and ~2 km deep, beginning 6 km from the magma injection zone on both ridge flanks (Fig. 3a). The associated horizontal deviatoric stresses exceed tens of MPas and reach the point of compressive Mohr-Coulomb failure, with stresses that peak ~15 km off-axis. This stress field is consistent with the occurrence of shallow, ridge-perpendicular reverse-faulting earthquakes near the summit of the ridge flanks (Fig. 1c, d).

The shallow compressive strain produced by unbending of the ridge flanks can be estimated through an order-of-magnitude approach, as the ratio of the compressive zone thickness D (~2 km in Fig. 3a) to the lithosphere's radius of curvature[33]. A simple unbending model[34, 20] relates the radius of curvature to the amplitude h of the axial relief (~1.5 km) and the flexural length scale α (~10 km). This yields a strain $\varepsilon \sim Dh/\alpha^2$ on the order of 0.03, large enough to leave a detectable signature in seafloor relief.

The bathymetric signature of unfaulting

At both the Northern Mid-Atlantic Ridge and Carlsberg Ridge, we detect a sharp break in the trend of cumulative fault offset vs. off-axis distance, at about 15 km, roughly co-located with the bands of compressive earthquakes (Fig. 2). The break in slope corresponds to a reduction in the apparent fraction T of tectonic extension by 0.06–0.1. We interpret this break in slope as a reduction of the average offset on abyssal hill bounding faults caused by cumulative reverse slip (Fig. 4a). To first order, T corresponds to the characteristic normal fault heave (the horizontal component of fault offset) divided by the characteristic fault spacing. Therefore, a decrease from $T = 0.13$ to $T' = 0.07$ (Fig. 2a) can represent a reduction in heave from ~400 m down to ~200 m for a population of faults evenly spaced by ~3 km, a scenario consistent with the morphology of the 54ºN segment of the Mid-Atlantic Ridge (Fig. 1c).

The Carlsberg and Northern Mid-Atlantic Ridge are not unique in hosting near-axis reverse-faulting earthquakes. Over a dozen more comparable events can be found throughout the Global CMT Catalog[35, 20], along the ultraslow-spreading Southwest Indian Ridge, the slow-spreading Mid-Atlantic Ridge and Carlsberg Ridge, as well as the intermediate-spreading Southeast Indian Ridge (Extended Data Figs. 1, 3). Based on low-resolution bathymetric and gravity data, ref. 20 attributed these events to unbending in the footwall of large-offset detachment faults, where small magnitude reverse seismicity had previously been documented[36]. This interpretation is however at odds with available high-resolution bathymetry data: out of the 13 ridge sections that have hosted reverse-faulting earthquakes and have been mapped with shipboard multibeam echosounders (Fig. 4b, Supplementary Tables 2, 3), ten display a magmatically robust morphology (in the sense of ref. 21) with symmetric, staircase-like abyssal hills bounded by short-offset faults (Extended Data Figs. 1, 3). While the other three do host scattered detachment faults, a systematic co-location with the reverse quakes is difficult to establish given the large location uncertainties of teleseismic events. Analyzing representative bathymetric profiles from all these ridge sections systematically yields a reduction in the apparent T fraction by 0.02–0.18 at distances ranging from ~10 to 30 km off-axis (Extended Data Figs. 1, 4, 5). In addition, revisiting a published database of 2157 normal faults identified along the intermediate-spreading Chile Ridge[24] —where we found no near-axis compressive event in the CMT catalog— yields a similar pattern at the scale of the entire ridge (Extended Data Figs. 6–8, Supplementary Tables 3, 4). There, T-T' ~0.07, but the shift occurs slightly closer to the ridge axis, within ~7 to ~16 km from the neovolcanic zone.

It is important to note that processes other than unfaulting could contribute to a reduction in apparent T fraction across the flanks of magmatically-robust ridge sections. These include sedimentation filling bathymetric lows and reducing the apparent amplitude of abyssal hills. Median sediment thickness however only increases by ~5 m per Myr of seafloor age[37–40]. Sedimentary infilling is thus unlikely to account for more than ~30 m of apparent offset reduction (e.g., T-$T' < 10^{-2}$) in areas of suspected unfaulting. On the other hand, gravitational mass wasting is known to alter the slopes of axis-facing fault scarps by maintaining them at or below the frictional angle of repose (~35º) through repeated rocksliding[41, 42]. The progressive nature of this process however appears at odds with the abruptness of the reduction in apparent T fraction (Fig. 2), unless the reduction marks the point where normal slip on abyssal hill faults ceases and mass wasting begins to overcome tectonic uplift. We do not favor this endmember interpretation because fault scarps appear to migrate across the unfaulting zone without any detectable change in their average slope (Extended Data Fig. 6d). Furthermore, axis-facing scarps on the fast-spreading East-Pacific Rise —which presumably experience gravitational mass wasting like other ridge sections–– show an increase in apparent T fraction ~17 km off-axis (Extended Data Fig. 9). This increase is readily explained by unbending away from an axial high[34] (T-T'<0), mirroring the unbending away from an axial valley (T-T'>0; Fig. 4a). We conclude that changes in apparent T fraction primarily reflect shallow flexural strains reworking the tectonic fabric of abyssal hills, as opposed to surface processes.

Available bathymetric data suggests that the unfaulting process as summarized in Fig. 4a primarily occurs at magmatically robust ($T \leq 0.2$) MOR sections with an axial valley flanked by pronounced ridge shoulders. It does not rule out the occurrence of unbending quakes in the footwall of oceanic detachments as proposed by ref. 20, but the impact of such events on ocean floor physiography is not as clear. As a measure of normal fault shortening, T-T' provides a proxy for the horizontal strain associated with shoulder compression. Its typical value (~0.07) however exceeds our initial order-of-magnitude estimate of $\varepsilon \sim 0.03$. One reason could be that the depth extent of reverse slip is greater than predicted by our numerical models (Fig. 3a), e.g., $\varepsilon \sim 0.07$ if D extends to ~5 km instead of ~2 km below seafloor, consistent with the depths of near-axis reverse-faulting earthquakes[20] (Supplementary Table 1). This could be achieved if the effective frictional strength of the shallow, compressed lithosphere was reduced, for example by the pressurization of pore fluids trapped in abyssal hill bounding faults. Supra-hydrostatic pore pressures could plausibly deepen the neutral bending plane in MOR shoulders down to ~5 km or deeper (Extended Data Fig. 10), and would also have the effect of narrowing the cross-axis extent of the unfaulting zone, contributing to a more abrupt decrease in apparent T (see Supplementary Information). Further, assuming D = 5 km and using the unfaulting distance (the position x_c of the sudden decrease in T) as a proxy for the flexural wavelength α to estimate the unfaulting strain ε yields a reasonable agreement with our measurements of T-T' across all candidate unfaulting sites (Fig. 4c).

Role of magmatic intrusions

The widespread bathymetric signature of abyssal hill unfaulting contrasts with its relative scarcity in the seismic record (Fig. 4b). The moment rate associated with extensional faulting at the axis straightforwardly scales as $\dot{M}_E \sim GUTH_0$ (per unit length along the ridge axis, with G the shear modulus and H_0 the thickness of the axial lithosphere; 43). The seafloor shortening rate in the ridge flanks can be estimated as the spreading half-rate times the reduction in fault heave per unit distance away from the axis, i.e., $\varepsilon U = (T\text{-}T')U$. Along the neutral plane located at depth D (Figs. 3a, 4a), there is no shortening. Consequently, the shortening rate averaged over the thickness of the compressive domain is $(T\text{-}T')U/2$. It follows that moment rate associated with reverse slip should scale as $\dot{M}_R \sim GU(T - T')D/2$, and $\dot{M}_R \,/\, \dot{M}_E \sim \frac{(T-T')D}{2TH_0}$. Assuming $D = H_0 \sim 5$ km, $T\text{-}T' \sim 0.07$ and $T \sim 0.15$ yields $\dot{M}_R \,/\, \dot{M}_E \sim 0.2$. Ref. 20 estimated the total moment rate of near-axis reverse-faulting events in the CMT catalog as the equivalent of 1.5 Mw5.5 earthquakes per year for the period 1985–2023, which is about 5% of the moment rate associated with normal-faulting events ($\dot{M}_R \,/\, \dot{M}_E \sim 0.05$). One explanation for this discrepancy could be that reverse slip in the shallow ridge flanks is more aseismic than normal slip on the edge of the axial valley. This would be consistent with supra-hydrostatic pore fluid pressures in the unfaulting zone, which increase the characteristic nucleation size of earthquakes and favor a regime where aseismic reverse slip transients account for greater cumulative displacements than reverse-faulting earthquakes[43–45].

The idea that flexural stresses alone cause reverse-faulting earthquakes only sporadically is consistent with the fact that the two clearest manifestations of the unfaulting process, the 2014 Carlsberg and 2022 Mid-Atlantic Ridge swarms, were plausibly triggered by a dike intrusion event[19]. In both instances, the reverse-faulting earthquakes were preceded by on-axis swarms of extensional seismicity, with a pattern of southward migration at ~0.2 m/s in the Atlantic case. Migrating seismicity at rates ~0.1–1 m/s has unambiguously been linked to dike propagation in Iceland and Ethiopia[46, 47], and similar swarms have been observed at magmatically active segments of the Juan de Fuca Ridge[48] and Gakkel Ridge[49]. It is thus likely that the initial swarm of extensional earthquakes was the manifestation of a magmatic fissure propagating along the ridge axis. Standard elastic dislocation modeling (Fig. 3b, Methods) shows that opening of a vertical dike between 4 and 10 km below the axial valley floor induces static Coulomb stress changes that promote normal slip on axial valley faults while promoting shallow reverse slip ~15 km off-axis. Magmatic fissures are typically ~1 meter wide at oceanic spreading centers[25]. A dike intrusion such as those inferred at the Carlsberg and Mid-Atlantic Ridge may thus represent a one-in-fifty year event that precipitated the occurrence of otherwise elusive unfaulting earthquakes (Fig. 4a). Although not necessary to drive reverse slip on MOR normal faults, magmatic intrusions may have been instrumental in revealing this fundamental component of seafloor spreading, which over geological time strongly reworks the fabric of the global ocean floor.

References from main text

1. Sykes, L.R. Mechanism of earthquakes and nature of faulting on the mid-oceanic ridges. *J. Geophys. Res.* **72**, 2131–2153 (1967)

2. Engeln, J.F., Wiens, D.A. & Stein, S. Mechanisms and depths of Atlantic transform earthquakes. *J. Geophys. Res.* **91**, 548–577 (1986)

3. Huang, P.Y., Solomon, S.C., Bergman, E.A. and Nabelek, J.L. Focal depths and mechanisms of Mid-Atlantic Ridge earthquakes from body wave-form inversion. *J. Geophys. Res.* **91**, 579–598 (1986)

4. Solomon, S.C., Huang P.Y. & Meinke, L. The seismic moment budget of slowly spreading ridges. *Nature* **334**, 58–60 (1988)

5. Menard, H.W. & Mammerickx, J. Abyssal hills, magnetic anomalies, and the East Pacific Rise. *Earth Planet. Sci. Lett.* **2**, 465–472 (1967)

6. Macdonald, K.C., Fox, P.J., Alexander, R.T., Pockalny, R. & Gente, P. Volcanic growth faults and the origin of Pacific abyssal hills. Nature **380**, 125–129 (1996)

7. Olive, J.-A., Behn, M.D., Ito, G., Buck, W.R., Escartín, J. & Howell, S. Sensitivity of seafloor bathymetry to climate-driven fluctuations in mid-ocean ridge magma supply. *Science* **350**, 6258 (2015)

8. Deffeyes, K.S., The axial valley: a steady state feature in the terrain. In *Megatectonics of continents and oceans*, Eds. Johnson, J. & Smith, B.C., 194–222, Rutgers Univ. Press (1970)

9. Osmaston, M.F. Genesis of ocean ridge median valleys and continental rift valleys. *Tectonophysics* **11**, 387–405 (1971)

10. Harrison, C.G.A. Tectonics of mid-ocean ridges. *Tectonophysics* **22**, 301–310 (1974)

11. Macdonald, K.C. Mid-Ocean Ridges: Fine Scale Tectonic, Volcanic and Hydrothermal Processes Within the Plate Boundary Zone. *Annual Review of Earth and Planetary Sciences* **10**, 155–190 (1982)

12. Needham, H.D., & Francheteau, J. Some characteristics of the rift valley in the Atlantic ocean near 36º48' North. *Earth Planet. Sci. Lett.* 22, 29–43 (1974)

13. Bergman, E.A. & Solomon, S.C. Source mechanisms of earthquakes near mid-ocean ridges from body waveform inversion: Implications for the early evolution of oceanic lithosphere. *J. Geophys. Res.* **89**, 11415–11441 (1984)

14. Fleitout, L. & Froidevaux, C., Tectonic stresses in the lithosphere. *Tectonics 2*, 315–324 (1983)

15. Wolfe, C.J., Bergman, E.A., & Solomon, S.C. Oceanic transform earthquakes with unusual mechanisms or locations: Relation to fault geometry and state of stress in the adjacent lithosphere. *J. Geophys. Res.* **98**, 16187–16211 (1993)

16. Turcotte, D.L. Are transform faults thermal contraction cracks? *J. Geophys. Res.* **79**, 2573–2577 (1974)

17. Behn, M.D., Lin, J. & Zuber, M.T. Evidence for weak oceanic transform faults. *Geophys. Res. Lett.* **29**, 2207 (2002)

18. Janin, A., Chamot-Rooke, N., Delescluse, M., Fournier, M., Olive, J.-A., Rabaute, A. et al. Tectonic evolution of a sedimented oceanic transform fault: The Owen Transform Fault, Indian Ocean. *Tectonics* **42**, e2023TC007747 (2023)

19. Cesca, S., Metz, M, Büyükakpınar, P. & Dahm, T. The energetic 2022 seismic unrest related to magma intrusion at the North Mid-Atlantic Ridge. *Geophys. Res. Lett.* **50** (2023)

20. Jackson, J. & McKenzie, D. Reverse-faulting earthquakes and the tectonics of slowly-spreading mid-ocean ridge axes. *Earth Planet. Sci. Lett.* **618** (2023).

21. Escartín, J., Smith, D. K., Cann, J., Schouten, H., Langmuir, C.H. & Escrig S. Central role of detachment faults in accretion of slow-spreading oceanic lithosphere. *Nature* **455**, 790-794 (2008)

22. Searle, R.C. & Laughton, A.S. Sonar studies of the Mid-Atlantic Ridge and Kurchatov Fracture Zone. *J. Geophys. Res.* **82**, 5313–5328 (1977)

23. Escartín, J., Cowie, P.A., Searle, R.C., Allerton, S., Mitchell, N.C., MacLeod, C.J. & Slootweg, A.P. Quantifying tectonic strain and magmatic accretion at a slow spreading ridge segment, Mid-Atlantic Ridge, 29°N. *J. Geophys. Res.* **104**, 10421–10437 (1999)

24. Howell, S., Ito, G., Behn, M. D., Martinez, F., Olive, J.-A. & Escartín, J. Magmatic and tectonic extension at the Chile Ridge: Evidence for mantle controls on ridge segmentation, *Geochem. Geophys. Geosyst.*, 17 (2016)

25. Qin, R. & Buck, W.R. Why meter-wide dikes at spreading centers? *Earth Planet. Sci. Lett.* **265**, 466-474 (2008)

26. Olive, J.-A. & Dublanchet, P. Controls on the magmatic fraction of extension at mid-ocean ridges. *Earth Planet. Sci. Lett.* **549** (2020)

27. Buck W.R., Lavier L.L., & Poliakov, A.N.B. Modes of faulting at mid-ocean ridges. *Nature* **434**, 719–723. (2005)

28. Behn, M.D. & Ito, G. Magmatic and tectonic extension at mid-ocean ridges: 1. Controls on fault characteristics. *Geochem. Geophys. Geosyst.* **9** (2008)

29. Tucholke B E, Behn M D, Buck W R, et al. Role of melt supply in oceanic detachment faulting and formation of megamullions. Geology, 2008, 36(6): 455-458.

30. Liu, Z. & Buck, W.R. Global trends of axial relief and faulting at plate spreading centers imply discrete magmatic events. *J. Geophys. Res.* **125**, e2020JB019465 (2020)

31. Liu, Z. & Buck, W.R. Magmatic controls on axial relief and faulting at mid-ocean ridges. *Earth Planet. Sci. Lett.* **491**, 226-237 (2018)

32. Qin, R. & Buck, W.R. Effect of lithospheric geometry on rift valley relief, *J. Geophys. Res.* **110** (2005)

33. Turcotte, D. L & Schubert, G. Geodynamics, 2nd edition, *Cambridge University Press* (2002)

34. Buck, W.R. Accretional curvature of lithosphere at magmatic spreading centers and the flexural support of axial highs. *J. Geophys. Res.* **106**, 3953–3960 (2001)

35. Ekström, G., Nettles, M. & Dziewonski, A.M. The global CMT project 2004-2010: Centroid-moment tensors for 13,017 earthquakes. *Phys. Earth Planet. Inter.* **200**, 1-9 (2012)

36. Parnell-Turner, R., Sohn, R.A., Peirce, C., Reston, T.J., MacLeod, C.J., Searle R.C. & Simão, N.M., Oceanic detachment faults generate compression in extension. *Geology* **45**, 923–926 (2017)

37. Mitchell, N.C., Allerton, S. & Escartín, J. Sedimentation on young ocean floor at the Mid-Atlantic Ridge, 29ºN. *Marine Geology* **148**, 1–8 (1998)

38. Ewing, J. & Ewing, M. Sediment distribution on the mid-ocean ridges with respect to spreading of the sea floor. *Science* **156**, 1590–1592 (1967)

39. Divins, D.L. Total sediment thickness of the world's oceans & marginal seas. NOAA National Geophysical Data Center, Boulder CO (2003)

40. Johnson, H.P. & Pruis, M.J. Fluid and heat from the oceanic crustal reservoir. *Earth Planet. Sci. Lett.* **216**, 565–574 (2003)

41. Tucholke, B.W., Stewart, K.W. & Kleinrock, M.C., Long-term denudation of ocean crust in the central North Atlantic Ocean. *Geology* **25**, 171–174 (1997)

42. Cannat, M., Mangeney, A., Ondréas, H., Fouquet, Y., & Normand, A. High-resolution bathymetry reveals contrasting landslide activity shaping the walls of the Mid-Atlantic Ridge axial valley. *Geochem. Geophys. Geosyst.* **14**, 996–1011 (2013)

43. Olive, J.-A. & Escartín, J. Dependence of seismic coupling on normal fault style along the Northern Mid-Atlantic Ridge. *Geochem. Geophys. Geosyst.* **17** (2016)

44. Liu, Y. & Rice, J.R. Spontaneous and triggered aseismic deformation transients in a subduction fault model. *J. Geophys. Res.* **112** (2007)

45. Mark, H.F., Behn, M.D., Olive, J.-A. & Liu, Y., Controls on mid-ocean ridge normal fault seismicity across spreading rates from rate-and-state friction models. *J. Geophys. Res.* **123** (2018)

46. Einarsson, P. & Brandsdóttir, B. Seismological evidence for lateral magma intrusion during the July 1978 deflation of the Krafla volcano in NE-Iceland *J. Geophys. Res.* **47**, 160–165 (1980)

47. Keir, D. et al. Evidence for focused magmatic accretion at segment centers from lateral dike injections captured beneath the Red Sea rift in Afar. *Geology* **37**, 59–62 (2009)

48. Bohnenstiehl, D. R., Dziak, R.P., Tolstoy, M., Fox, C. & Fowler, M. Temporal and spatial history of the 1999–2000 Endeavor seismic series, Juan de Fuca Ridge. *Geochem. Geophys. Geosyst.* **5**, Q09003 (2004)

49. Tolstoy, M., Bohnenstiehl, D.R., Edwards, M. & Kurras, G. The seismic character of volcanic activity at the ultra-slow spreading Gakkel Ridge, *Geology* **29**, 1139–1142 (2001)

50. Skolotnev, S.G. et al. Crustal accretion along the Northern Mid-Atlantic Ridge (52º–57ºN): Preliminary results from expedition V53 of R/V Akademik Sergey Vavilov. *Ofioliti* **48**, 13–30 (2023)

Main figure captions

Figure 1 | Swarms of normal and reverse seismicity at two slow-spreading mid-ocean ridges. **a.** Bathymetry of the 54ºN segment of the Northern Mid-Atlantic Ridge[50], showing relocated earthquakes from the 2022 swarm. Red and blue beachballs show normal and reverse mechanisms, respectively. NTO: Non-transform offset. AV: Axial valley. **b.** Bathymetry of the Carlsberg Ridge near 6ºN, with relocated 1990–2020 seismicity (Global CMT Catalog[35]). Shading reveals zones with multibeam data (visible fault scarps) vs. interpolated bathymetry (textureless). **c.** Topographic cross-section along dotted line in panel a, with fault scarps shown in red (west side) and yellow (east side). Blue bars indicate projected location of reverse-faulting events. **d.** Topographic cross-section along dotted line in panel b: closest available transect with shipboard bathymetry. V.E. = vertical exaggeration.

Figure 2 | Tectonic strain and the bathymetric signature of unfaulting. Plots of cumulative fault heave vs. distance from the axis for **a.** the Mid-Atlantic Ridge at 54ºN, and **b.** the Carlsberg Ridge at 6ºN. Blue bands mark location of reverse-faulting events. Black lines show best fitting piece-wise linear function, with slope T (the tectonic fraction of plate separation) near the ridge axis, and slope T' further off-axis.

Figure 3 | The stress state of mid-ocean ridge shoulders. **a.** Cross-section of the horizontal deviatoric stress in a 2-D numerical model of seafloor spreading developing an axial valley and symmetric shoulders[30, 31]. See text for meaning of symbols. **b.** Change in shear stress ($\Delta\tau$) resolved on 45º-dipping faults (>0 and <0 indicates normal and reverse motion, respectively) induced by 1 meter of dike opening (purple line), shown only in areas where the Coulomb stress change (ΔCFS) brings faults closer to failure. Black line shows relief of the 54º segment of the Mid-Atlantic Ridge.

Figure 4 | Mid-ocean ridge unfaulting. **a.** Cartoon showing the shallow flexural compression of mid-ocean ridge flanks, and the occasional triggering of reverse slip by a magmatic intrusion. Red and blue stars represent extensional and reverse-faulting earthquakes. Inset illustrates the depth-dependent stress state of unbending lithosphere, with shallow compression (blue) and deep extension (red). **b.** Spilhaus projection map of mid-ocean ridge strike-slip and normal-faulting earthquakes from the Global CMT catalog. Blue dots show reverse-faulting earthquakes that occurred in areas with a documented signature of bathymetric unfaulting (see Supplementary Information). **c.** Relationship between the change in apparent T fraction (T-T') and unfaulting strain (ε), estimated as the product of axial relief (h) by the depth of the unfaulting zone (D, here assumed to equal 5 km everywhere) divided by the unfaulting distance x_c (here used as a proxy for flexural wavelength α) squared. Error bars are derived from the non-linear least squares fit to the cumulative offset plots (e.g., Fig. 2, see Methods). Size of the symbols scales with x_c.

Methods

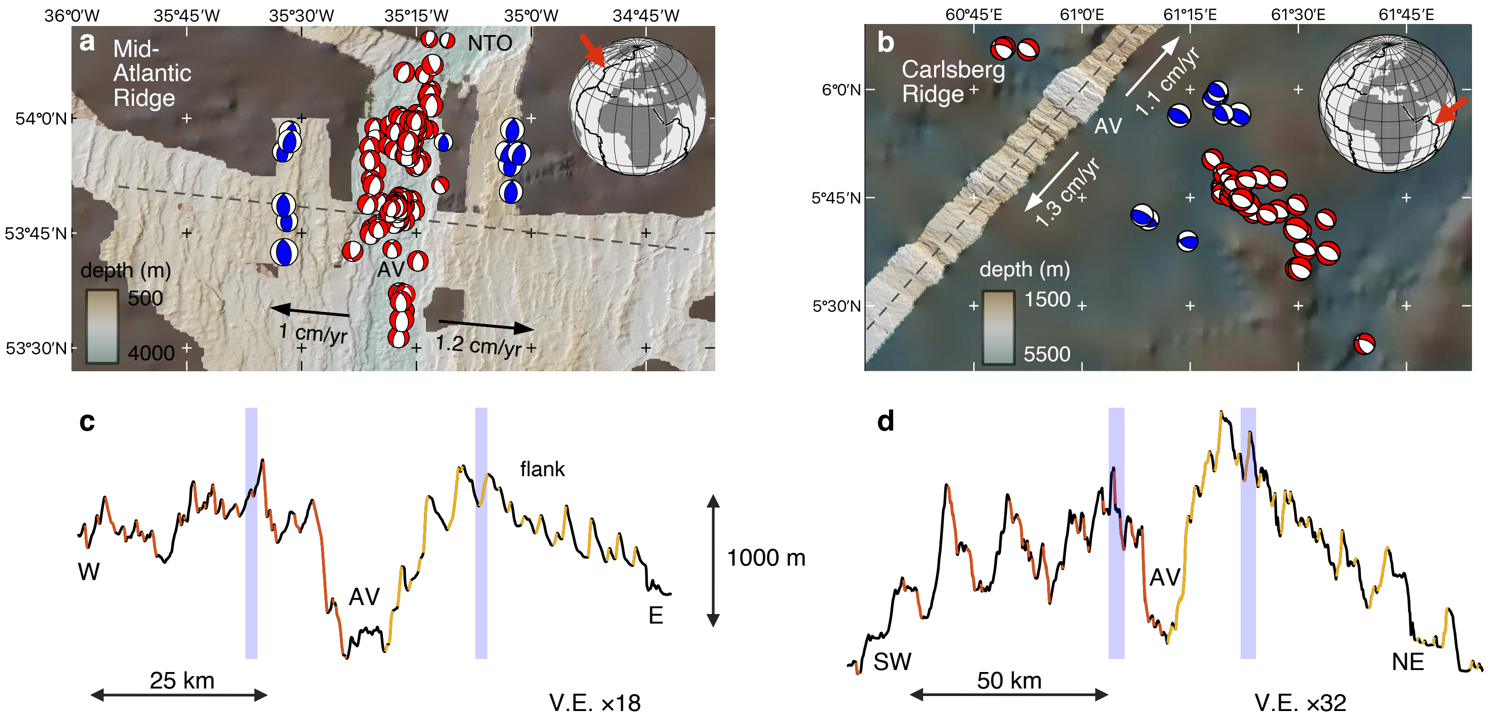

a
Mid-
Atlantic
Ridge
36°0′W
35°45′W
35°30′W
35°15′W
35°0′W
34°45′W
54°0′N
53°45′N
53°30′N
NTO
AV
depth (m)
500
4000
1 cm/yr
1.2 cm/yr
b
Carlsberg
Ridge
60°45′E
61°0′E
61°15′E
61°30′E
61°45′E
6°0′N
5°45′N
5°30′N
AV
1.1 cm/yr
1.3 cm/yr
depth (m)
1500
5500
c
flank
W
AV
E
1000 m
25 km
V.E. ×18
d
SW
AV
NE
50 km
V.E. ×32

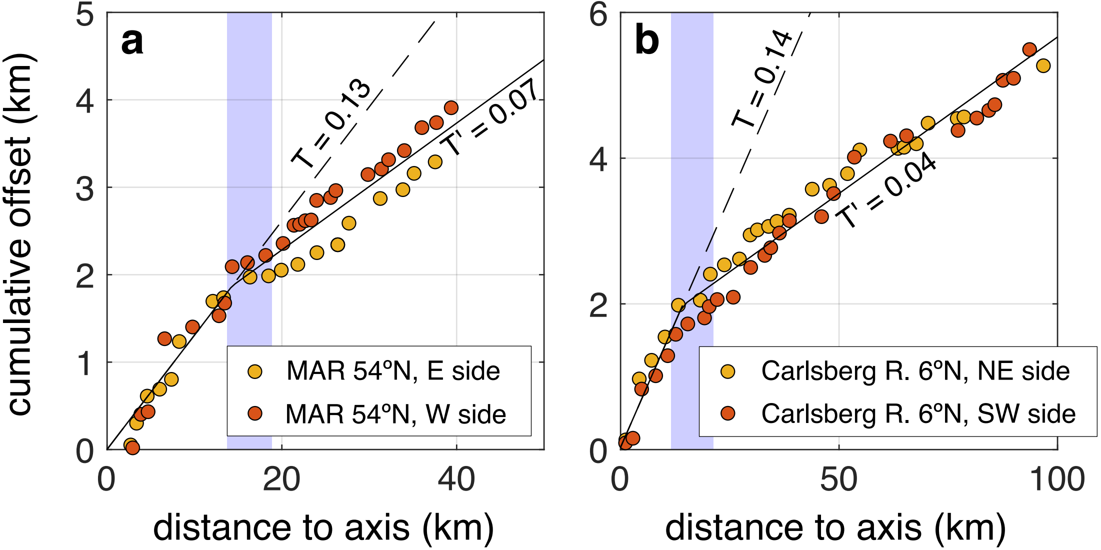

a
b
cumulative offset (km)
distance to axis (km)
T = 0.13
T' = 0.07
T = 0.14
T' = 0.04
MAR 54ºN, E side
MAR 54ºN, W side
Carlsberg R. 6ºN, NE side
Carlsberg R. 6ºN, SW side
0
1
2
3
4
5
20
40
0
2
4
6
50
100

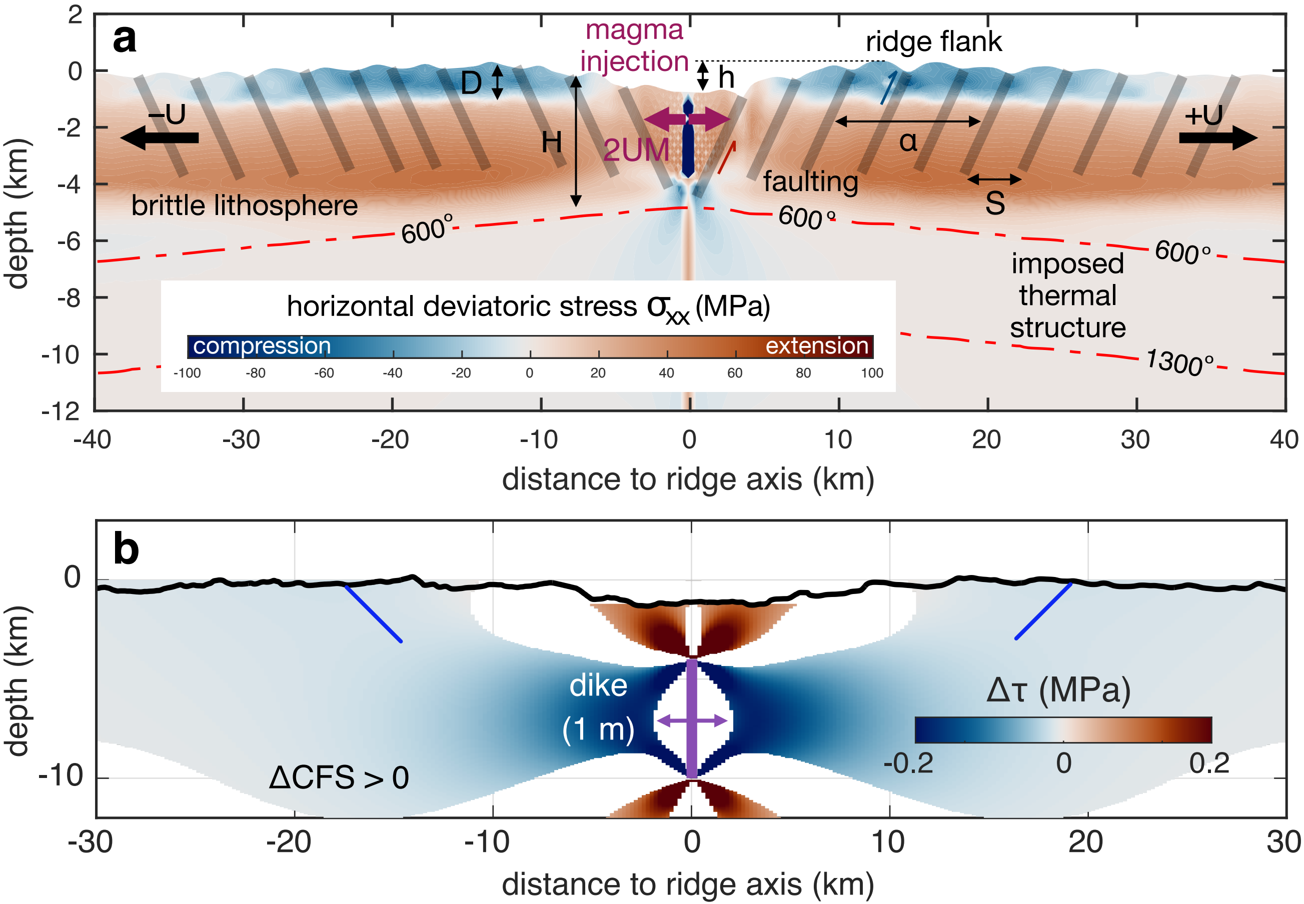

a
magma
injection
ridge flank
D
h
H
−U
+U
2UM
α
faulting
S
brittle lithosphere
600°
600°
600°
imposed
thermal
structure
1300°
horizontal deviatoric stress σ_{xx} (MPa)
compression
extension
-100 -80 -60 -40 -20 0 20 40 60 80 100
depth (km)
2 0 -2 -4 -6 -8 -10 -12
-40 -30 -20 -10 0 10 20 30 40
distance to ridge axis (km)
b
0
-10
dike
(1 m)
Δτ (MPa)
-0.2 0 0.2
ΔCFS > 0
depth (km)
-30 -20 -10 0 10 20 30
distance to ridge axis (km)

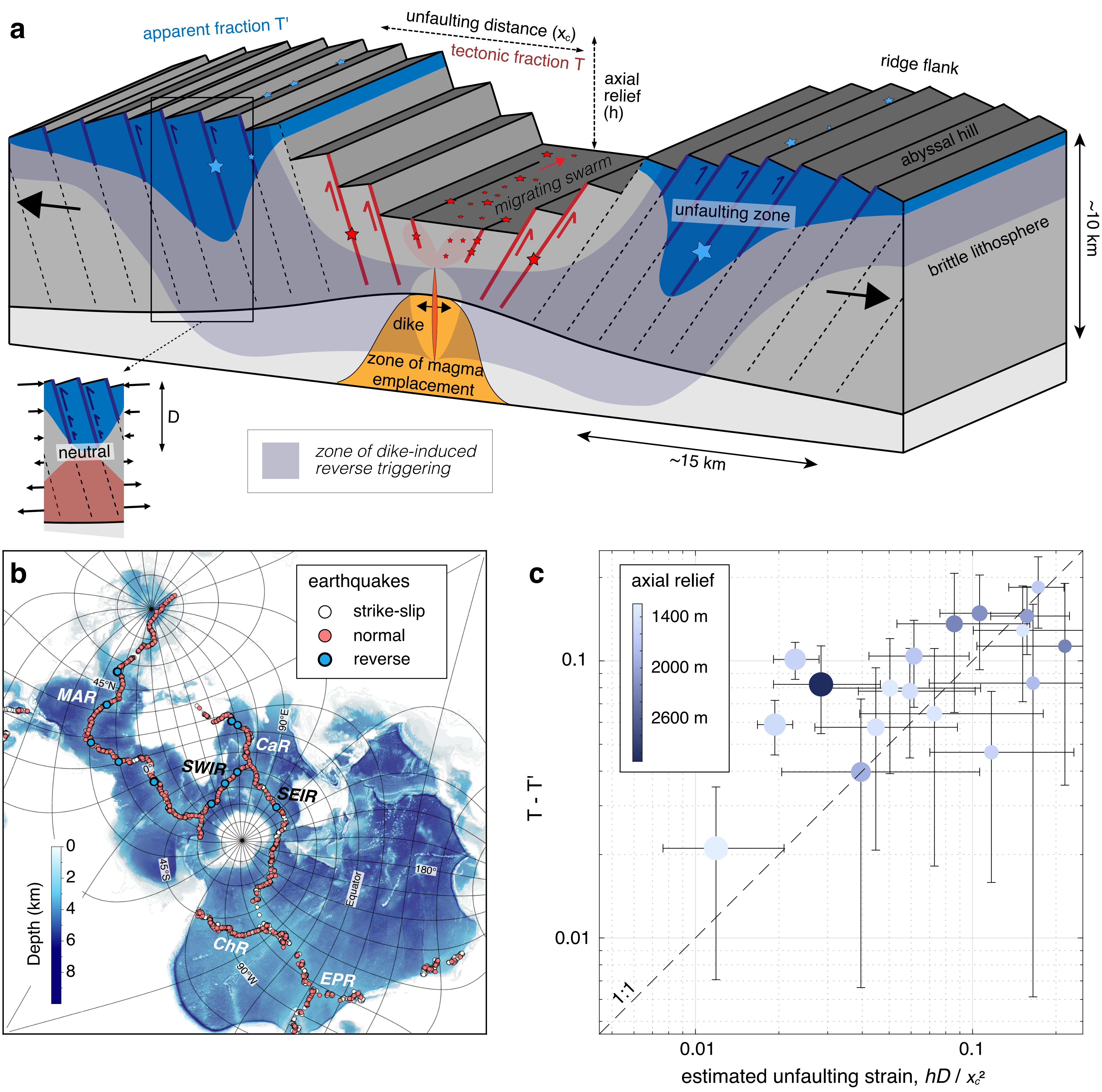
a
apparent fraction T'
unfaulting distance (x_c)
tectonic fraction T
axial relief (h)
ridge flank
abyssal hill
migrating swarm
unfaulting zone
brittle lithosphere
~10 km
dike
zone of magma emplacement
D
neutral
zone of dike-induced reverse triggering
~15 km
b
earthquakes
strike-slip
normal
reverse
MAR
SWIR
CaR
SEIR
ChR
EPR
45°N
90°E
0°
45°S
180°
Equator
90°W
Depth (km)
0
2
4
6
8
c
axial relief
1400 m
2000 m
2600 m
T - T'
0.1
0.01
1:1
estimated unfaulting strain, hD / x_c^2

Earthquake locations and mechanisms

Earthquakes on the northern Mid-Atlantic Ridge are far from seismographic stations, and event detection is therefore limited to moderate and larger earthquakes ($M > 4.0$). In this study, we rely primarily on hypocenters reported by the National Earthquake Information Center (NEIC, https://www.usgs.gov/programs/earthquake-hazards/national-earthquake-information-center-neic). The NEIC routinely reports hypocenters for earthquakes M ≥ 4.5 in this area, but only rarely for events smaller than M 4.2. To complement the NEIC hypocenters, we make use of surface-wave detections and locations calculated using intermediate-period (35-150 s) surface waves recorded on the Global Seismographic Network (GSN) using a global grid search[51]. The threshold for the surface-wave detector is ~4.7, but occasionally an event of that size will be missed in the NEIC catalog.

Uncertainties for earthquake locations based on teleseismic P-wave arrivals are typically 10–20 km[52]. They can be even larger for surface-wave detections[51], which gives rise to significant scatter in earthquake epicenters. We relocate them using cross-correlations of their Rayleigh and Love waveforms, without correcting for specific surface wave radiation patterns[53]. This yields clearly defined bands of seismicity with relative location uncertainty smaller than 2 km, based on the misfit of the very large numbers of differential travel times (Supplementary Table 1). Empirical location estimates, based on inversions of subsets of the available data, are smaller than ~5 km for all but five of the earthquakes. Because the absolute location of the earthquakes is not well constrained, we shift their latitudes by 0.054º (~6 km) to the West in a manner that centers the central band of seismicity over the neovolcanic axis as identified from bathymetric maps of the 54ºN segment (Fig. 1a).

We calculate focal mechanisms for these events using the centroid-moment-tensor algorithm employed in the Global CMT (GCMT) Project[35, 54]. Long-period (>40 s) body- and surface-wave seismograms recorded on the GSN are matched to estimate the six elements of the moment tensor, and an earthquake centroid location in time and space. We follow the procedure used in the standard GCMT processing[35], and attempt analysis of all events with at least one reported magnitude of 4.7 or larger. The focal mechanisms for all earthquakes shown here are available in the GCMT catalog.

Between September 26, 2022 and January 30, 2023, 125 events yield stable and robust moment-tensor results, using the same quality criteria used in the standard GCMT processing. Fig. 1a shows the focal mechanisms of the 125 earthquakes plotted at their reported epicenters. A majority of the events (n = 113) have normal-faulting geometries, with the remaining events (n = 12) having reverse mechanisms. The fault strikes of both normal and reverse mechanisms are generally North–South, with some variability. Fault dips also show variability. It is likely that much of the variation can be attributed to uncertainties in the moment-tensor estimates as many events are small (M < 5) and the dip-slip components of the moment tensor are difficult to constrain for shallow sources using long-period seismograms[55].

The 47 earthquakes shown in Fig. 1b occurred between August 10, 1990 and June 14, 2019 on the Carlsberg Ridge. These have been analyzed previously as part of the GCMT project. Here we relocated them using the surface wave cross-correlation method described above, again yielding a clear central band of extensional events (Supplementary Table 1). All earthquake locations were shifted by 0.0581º (~6 km) to the East and by 0.0436º (~5 km) to the North to align the central band with the ridge axis.

Hypocenter depths for the 2022 Mid-Atlantic Ridge swarm

Hypocenter depths are not well constrained in standard location algorithms that mainly rely on first-arriving P waves. Uncertainties are typically on the order of 10 km. The long-period body and surface waves used in the CMT analysis are similarly insensitive to the earthquake depth. To obtain better depth estimates, we examine the P wave waveforms recorded at teleseismic distances. At these distances, the first-arriving P wave is followed by phases reflected off the surface of the Earth, or off internal boundaries above the source. The delay times of the most prominent reflections pP and sP can sometimes be used to infer a depth when the duration of the source is shorter than the difference in the travel time of the two phases. For very shallow earthquakes, the reflected phases overlap the direct phase, creating a complicated waveform.

We examined P-wave waveforms for the M5.7 normal-faulting earthquake on September 26 and the three largest reverse-faulting earthquakes on September 29 (M5.8), October 1 (M5.9) and November 29, 2022 (M5.5). The waveforms show P-wave polarities consistent with the GCMT focal mechanisms. When the pulses are filtered to reflect ground displacement it becomes clear that at many stations the initial P-wave onset is followed nearly immediately (within 1–3 seconds) by an arrival of opposite polarity. We interpret this as interference by ocean-bottom and ocean-surface reflected phases. A delay of ∼1 second between the P-wave onset and the change of displacement polarity observed at some stations is consistent with very shallow earthquake depth (<5 km). To obtain a more robust depth estimate it is necessary to model the interference of the direct and reflected phases. We model the broadband teleseismic P wave using the method of ref. 56. In this technique, the broadband P-wave waveforms are synthesized in a layered elastic structure including a water layer. The depth, focal mechanism, and moment-rate function are varied to obtain, in a least-squares sense, the best fit between observed and synthetic waveforms. The CMT solution is used as a soft constraint on the focal mechanisms to stabilize the inversion. We used a simple elastic model with an eight-kilometer-thick oceanic crust overlain by an ocean layer. We estimated the water depth at the locations of each of the four earthquakes from the bathymetry. For the normal-faulting earthquake, we used a water depth of 2000 meters (bottom of the axial valley), and for the reverse-faulting earthquakes we used depths between 1200 and 1500 meters (top of the ridge flanks).

The results from the broadband P-wave inversions are consistent with the qualitative interpretation of the polarity change as resulting from early reflected phases. The best-fitting point-source focal depths below the ocean surface range between 2.7 and 4.2 km, corresponding to depths in the top 3 km in the crust. In the inversion, these depths are primarily constrained by the early part of the waveform, and the observed early polarity change. Since the earthquake durations are longer than the delay between the direct and reflected phases, the depth of the full rupture may be larger than the estimated point-source depth. The inversion results constrain the initial part of the rupture to have occurred at very shallow depth in the crust (<3 km). The later part of the rupture may have extended deeper. A summary of our depth estimates is included in Supplementary Table 1.

Fault strain from bathymetric analyses

To estimate the fraction of plate separation T taken up by slip on major faults, we use a standard method to calculate the cumulative vertical displacement (throw) of faults[22–24]. This method consists of identifying fault scarps in ridge-normal transects of high-resolution shipboard bathymetry and summing their vertical offsets as a function of along-profile distance. We specifically select steep axis-facing slopes bounded by sharp breaks (Fig. 1c, d), to minimize confusion with volcanic features[57]. Because of mass wasting and other seafloor reworking processes[41, 42], the vertical offset on a scarp is generally considered a more reliable estimator of vertical fault offset than its horizontal extent[58]. We therefore use scarp throw as a proxy for fault throw, and divide it by the tangent of the assumed fault dip to assess fault heave. Numerical models suggest that MOR faults rapidly rotate from their steep initial angles (>50º) to shallower dips closer to 45º (59), consistent with the focal mechanisms in our catalog. We therefore assume a dip of 45º for all faults in this study. We then construct plots of the cumulative horizontal offset on faults as a function of distance to the axis (the position of the mid-point of each fault scarp). These typically show a linear trend with slope T close to the axis, and a sharp decrease in slope ($T' < T$) ~15 km off-axis. It should be noted that assuming a dip of 45º only affects the absolute value of T, which can be straightforwardly adjusted to account for a different fault dip. We use a non-linear least-squares method to fit a continuous, piece-wise linear function with slopes T and T' before and after a cutoff-distance x_c, with y-intercept y_0, to all our plots of cumulative offset vs. distance. The only constraint enforced on T, T', and y_0 is that they are positive, while x_c must be greater than the distance of the first fault to the axis. Bathymetric data for the 54ºN segment of the Mid-Atlantic Ridge is from ref. 50.

Candidate unfaulting events across the global MOR system

We searched the Global CMT catalog[35] for reverse-faulting events indicative of ridge-normal compression within ~50 km of a MOR axis[20]. We retained those located in areas with sufficient shipboard bathymetric coverage —as compiled in the NCEI (NOAA) and GMRT (LDEO/NSF) repositories, and by additional sources listed in the corresponding figure captions— to perform the fault strain analysis described in the above section. These earthquakes are plotted in Fig. 4b and listed in Supplementary Table 2. They occurred in 13 sections of the Southwest Indian Ridge (SWIR), Carlsberg Ridge, Mid-Atlantic Ridge (MAR), and Southeast Indian Ridge (SEIR), spanning ultraslow, slow and intermediate spreading rates. Corresponding maps are shown in Fig. 1 and Extended Data Figs. 1 and 3. Ten of these 13 sections feature regularly spaced abyssal hills bounded by steep axis-facing normal faults, and can be unambiguously classified as magmatically-robust following the criteria of ref. 21. The other three (Extended Data Fig. 3d, e, h) feature corrugated surfaces typical of large-offset detachment faults, although the reverse-faulting earthquakes typically occurred beneath a terrain dissected by steep, closely-spaced faults (within a typical location uncertainty of 10–20 km). This is evident from the bathymetric profiles we gathered in each location, which are plotted in Extended Data Figs. 4 and 5. Results of our strain analyses are compiled in Supplementary Table 3. All sections showed evidence for unfaulting, with T-T' averaging 0.09 ± 0.04 (Fig. 4c).

Lack of unfaulting near an axial high: the East Pacific Rise at 9º30'N

We performed one additional strain analysis in a bathymetric profile across the fast-spreading East Pacific Rise (EPR) at 9º30'N (Extended Data Fig. 9). Of all the ridge sections we analyzed, this is the only one where the non-linear least-squares fit yielded a value of T' (0.04) greater than T (0.01). This is consistent with the model of ref. 34, in which lithospheric unbending away from an axial high results in shallow extension. This configuration can be viewed as reciprocal to the shallow compression induced by unbending away from an axial valley, which drives unfaulting (Fig. 3a). It further suggests that the decrease in apparent T fraction observed in all profiles that straddle ridge valley shoulders cannot be solely due to seafloor reworking processes such as mass wasting or sedimentation. This is because these processes are likely active at the EPR, where the apparent T fraction increases away from the ridge axis.

Numerical modeling of mid-ocean ridge relief and stress

Using the approach of ref. 30 we conducted 2-D numerical simulations of magmatic injection and fault growth at an idealized mid-ocean ridge with a fixed thermal structure. This approach builds on a series of spreading center models[7, 27, 29] that used FLAC (Fast Lagrangian Analysis of Continua), an explicit hybrid finite-element and finite-difference technique, to solve the equations of mass, momentum and energy conservation in a visco-elastic-plastic continuum. This method is well suited to simulating localized deformation, approximating faulting, and is described in detail elsewhere[60–62].

We consider deformation in a 2-D model domain 150 km wide and 20 km deep (Fig. 3a). The top boundary is stress free and the bottom boundary is a Winkler foundation, simulating flotation on an inviscid substrate with a mantle density. The sides are pulled at a constant velocity (full rate: $2U$ = 2.5 cm/yr) and crustal material is added via diking and lower crustal intrusion at the model center as described below. Regridding of the distorted Lagrangian mesh occurs regularly, and returns the base and sides of the model domain to their original positions. Mantle material is added or subtracted at the base during re-gridding.

Both the crustal and mantle material are assigned a visco-elastic–plastic rheology with a viscosity that reflects a power law relating strain rate to the differential stress to the power n = 3, and an Arrhenius dependence on temperature. The parameter values are those of dry diabase[63], which ensures that the region cooler than ~600ºC (lithosphere) behaves essentially elasto-plastically. Brittle-plastic deformation is described by a Mohr-Coulomb failure criterion with a friction coefficient of 0.63 and initial cohesion of 25 MPa. When this yield criterion is met, the material weakens with strain beyond yield, leading to the localization of brittle deformation in model fault zones. Following previous work that simulated both bending and stretching related faulting[27], we consider 2 phases of strain weakening. 10 MPa of cohesion loss occurs over 1% of plastic strain, followed by 13 MPa of additional cohesion loss over 30% of strain. Our simulations do not account for the possibility of tensile failure. The model elements are 250 m wide and the fault zones in the model are typically ~4 elements wide[62]. The amount of fault slip necessary for total fault weakening (30% strain) is thus ~300 m. Both the crust and mantle are assigned a Young's modulus of 30 GPa and a Poisson's ratio of 0.25.

For simplicity, the thermal structure was fixed for the model shown in Fig. 3a, although similar models allowing self-consistent evolution of the thermal structure were used by ref. 31 to compare simulations with observed axial relief and faulting patterns as functions of spreading rate and crustal thickness. For the case shown in Fig. 3a, the seafloor was set to 20°C and the depth of the 600°C isotherm is set to 5 km at the ridge axis, and increases to 7 km, 40 km away from the axis. Temperature increases linearly with depth from the seafloor to the 600 ºC isotherm. It also increases linearly between the 600ºC and 1300ºC isotherms, but with five times the vertical temperature gradient. Temperature is capped at 1300ºC throughout the deeper parts of the model.

Dike intrusions accommodate the separation of plates at the spreading axis with a uniform average opening rate described by the M parameter (the fraction of plate spreading accommodated by diking as defined by ref. 27), such that the dike opening rate in the numerical model is defined as $2UM$. Instead of using a constant value for M, we follow the analysis of ref. 30 and relate it to crustal thickness (H_C) and on-axis lithosphere thickness (H_L) as follows:

$$M = \frac{H_C}{H_L + 0.5H_G}. \qquad (1)$$

In the above equation, H_G is the thickness of the magma column intruded into the asthenosphere due to the excess pressure associated with the development of the axial relief[30], and can be expressed as:

$$H_G = 0.25H_L + 0.5\sqrt{\frac{9}{4}{H_L}^2 + \frac{6P_{DL}H_L}{(\rho_c - \rho_f)g}}, \qquad (2)$$

where ρ_c is the density of the crust, ρ_f is the density of the magma, and P_{DL} is the driving pressure needed to open a meter-wide dike. In the simulation shown in Fig. 3a, H_C is 7 km, ρ_c and ρ_f are set to 3000 kg/m^3 and 2700 kg/m^3, and P_{DL} is 10 MPa. We further prescribe minor oscillations in the amount of magma delivered to dikes, implemented as:

$$H_C(t) = H_C + \Delta M\, H_C \sin(2\pi\, \omega\, t). \qquad (3)$$

In equation (3), ΔM and $1/\omega$ are the amplitude and period of the magma supply fluctuations, set to 0.15 and 0.2 Myr respectively. $H_C(t)$ is then used in equation (1) to compute temporal fluctuations in M. These small fluctuations are set to enable the regular growth of normal faults that are evenly spaced by ~3 km.

Elastic stress changes caused by a dike intrusion

We calculate the stress changes caused by 1 meter of uniform opening on a vertical, 6 km tall by 50 km long rectangular dislocation embedded in an elastic half-space. The calculation is carried out with the MATLAB routines of ref. 64, which allow us to mesh the dike with two triangular dislocations. The top of the dike is set at 4 km below the surface. The Young's modulus and Poisson's ratio of the material are set to 10 GPa and 0.25, respectively[65]. We compute the change in Coulomb Failure Stress[66] on 45º-dipping receiver faults striking parallel to the dike, assuming a friction coefficient of 0.6. Wherever this stress change is positive, faults are brought closer to failure. We assess their favored sense of slip by calculating their resolved shear stress, with the convention of negative shear stress indicating reverse motion. Results are shown in Fig. 3b. Because of the linearity of the problem, all stresses can be thought of as normalized by meter of opening on the axial dike. We note that the compressive stress changes imparted by diking across the ridge shoulders are ~100 times smaller than the absolute compressive stresses imparted by unbending (Fig. 3). Dike-induced compression is thus not sufficient to reverse the sense of slip on abyssal hill bounding faults, but could plausibly precipitate failure on faults already close to compressive yielding. Finally, it is important to note that the assumption of a homogeneous elastic half-space is warranted for rapid deformation events, but likely overestimates stress changes particularly if low-viscosity lower crust / asthenosphere can rapidly relax some of these stresses.

Data Availability

All bathymetric data used in this study are from the published literature as referenced[50, 67, 68], or openly available in the GMRT (https://www.gmrt.org/) / NOAA-NCEI (https://www.ncei.noaa.gov/maps/bathymetry/) repositories. The fault scarp dataset of ref. 24 is provided in Supplementary Table 4. Earthquake data are from the CGMT Catalog (https://www.globalcmt.org/CMTsearch.html), except for earthquake relocations, which are provided in Supplementary Table 1.

Code Availability

The simulation shown in Fig. 3a was run with the version of the FLAC code[60] developed by refs. 30 and 31. This code and the corresponding visualization scripts are available from the corresponding author upon reasonable request. The stress calculations shown in Fig. 3a were done with the code openly distributed with ref. 64.

References only cited in methods section

51. Ekström, G., Global detection and location of seismic sources using surface waves. *Bull. Seism. Soc. Am.* **96**, 1201–1212 (2006)

52. Smith, G.P & Ekström, G. Interpretation of earthquake epicenters and CMT centroid locations, in terms of rupture length and direction, *Phys. Earth Planet. Inter.* **102**, 123–132 (1997)

53. Howe, M., G. Ekström, and M. Nettles, Improving relative earthquake locations using surface-wave source corrections, *Geophys. J. Int.* **219**, 297–312 (2019)

54. Dziewonski, A.M., Chou T.-A. & Woodhouse, J.H. Determination of earthquake source parameters from waveform data for studies of global and regional seismicity. *J. Geophys. Res.* **86**, 2825-2852 (1981)

55. Ekström, G. & Dziewonski, A.M. Centroid-moment tensor solutions for 35 earthquakes in Western North America (1977-1983). *Bull. Seism. Soc. Am.* **75**, 23–39 (1985)

56. Ekström, G. A very broad band inversion method for the recovery of earthquake source parameters. *Tectonophysics* **166**, 73–100 (1989)

57. Escartín, J. & Olive, J.-A. Mid-Ocean Ridges and their Geomorphological Features. *Treatise on Geomorphology (2nd edition)*, 847-881 (2022)

58. Hughes, A., Escartín, J., Olive, J.-A., Billant, J., Deplus, C., Feuillet, N., Leclerc, N. & Malatesta, L.C. Quantification of gravitational mass wasting and controls on submarine scarp morphology along the Roseau fault, Lesser Antilles. J. *Geophys. Res. Earth Surface* **126** (2021)

59. Olive, J.-A. & Behn, M.D. Rapid rotation of normal faults due to flexural stresses: An explanation for the global distribution of normal fault dips, *J. Geophys. Res.* **119** (2014)

60. Cundall, P.A. Numerical experiments on localization in frictional materials. *Ingenieur Archiv* **59**, 148–159 (1989)

61. Poliakov A.N.B., Podladchikov Y. & Talbot C. Initiation of salt diapirs with frictional overburdens: numerical experiments. *Tectonophysics* **228**, 199–210 (1993)

62. Lavier L.L., Buck W.R. & Poliakov A.N.B. Factors controlling normal fault offset in an ideal brittle layer. *J. Geophys. Res*. **105**, 23431–23442 (2000)

63. Mackwell S.J., Zimmerman M.E. & Kohlstedt D.L. High-temperature deformation of dry diabase with application to tectonics on Venus. *J. Geophys. Res*. **103**, 975–984 (1998)

64. Meade, B.J. Algorithms for the calculation of exact displacements, strains, and stresses for triangular dislocation elements in a uniform elastic half space. *Computers and Geosciences* **33**, 1064–1075 (2007)

65. Heap, M. J. et al. Towards more realistic values of elastic moduli for volcano modelling. *Journal of Volcanology and Geothermal Research* **390**, 106684 (2020)

66. King, G.C.P., Stein, R.S. & Lin, J. Static stress changes and the triggering of earthquakes. *Bull. Seis. Soc. Am.* **84**, 935–953 (1994)

67. Maia, M. COLMEIA cruise. RV L'Atalante. doi.org/10.17600/13010010 (2013)

68. Maia, M. et al. Extreme mantle uplift and exhumation along a transpressive transform fault. *Nat. Geosci.* **9**, 619–623 (2016)

Acknowledgements

G.E. received support from the Consortium for Monitoring, Technology, and Verification under the Department of Energy National Nuclear Security Administration Award Number DE-NA0003920. Z.L. was funded by the JLU Science and Technology Innovative Research Team Program (No. 2021TD-05). M.B. was supported by the ISblue project (Interdisciplinary graduate school for the blue planet: ANR-17-EURE-0015) co-funded by a France 2030 / Investissement d'Avenir grant from the French government. We thank our editor and reviewers for their insightful feedback. We also thank I. Grevemeyer, S. Cesca, S. Solomon and A. Janin for helpful discussions. J. Chen and L.C. Malatesta provided valuable assistance with figure design. Lastly, we thank S. Skolotnev and M. Ligi for providing the MAR 54ºN bathymetric data.

Author contributions

J.-A.O. designed the study, conducted the bathymetric analyses with J.E. and M.B., carried out the elastic stress modeling, and wrote the initial manuscript. G.E. compiled and analyzed the earthquake data. W.R.B. and Z.L. designed the models of ridge flank flexure. All authors discussed and analyzed the results, and provided feedback on the manuscript.

Additional information

Supplementary Information is available for this paper. Correspondence and requests for materials should be addressed to J.-A.O. at olive@geologie.ens.fr. Reprints and permissions information is available at www.nature.com/reprints. The authors declare no competing interests.

Extended data figure captions

Extended Data Figure 1 | Examples of near-axis compression at mid-ocean ridges. (a) Bathymetric map of the Southeast Indian Ridge (SEIR) near 115ºE, with focal mechanisms from the CMT catalog. **(b)** Bathymetric map of the Mid-Atlantic Ridge (MAR) south of the Marathon transform fault (TF), with focal mechanisms from the CMT catalog. **(c)** Bathymetric profile across the SEIR (dashed line in panel a), with colored segments indicating fault scarps. **(d)** Cumulative fault heave vs. distance from the axis for the southern (red) and northern (yellow) sides of the SEIR, with best-fitting piece-wise linear functions shown as dashed lines ($T = 0.13$, $T' = 0.05$ on the South side; $T = 0.09$, $T' = 0.07$ on the North side). **(e)** Bathymetric profile across the western flank of the MAR (dashed line in panel b), with colored segments indicating fault scarps. **(f)** Cumulative fault heave vs. distance from the axis for the western side of the MAR, with best-fitting piece-wise linear function shown as dashed lines ($T = 0.21$, $T' = 0.08$).

Extended Data Figure 2 | The 2022 Northern Mid-Atlantic Ridge and 2014 Carlsberg Ridge seismic sequences. Latitude and moment magnitude of earthquakes, color-coded by mechanism (blue: reverse faulting, red: normal faulting) and location, throughout the **(a–d)** 2022 MAR sequence and (**e–h**) 2014 Carlsberg Ridge sequence.

Extended Data Figure 3 | Examples of near-axis reverse-faulting earthquakes at mid-ocean ridges. Bathymetric maps, reverse focal mechanism and profile used for strain analyses at **(a)** MAR 0º50'N near the St. Paul transform fault[67, 68]; **(b)** MAR 7º50'S; **(c)** MAR 34º50'N; **(d)** Carlsberg Ridge 9º45'N; **(e)** MAR 1º20'S; **(f)** SWIR 18º30'E; **(g)** MAR 17ºS; **(h)** SWIR 43ºE near the Discovery II transform fault; and **(i)** SWIR 57ºE.

Extended Data Figure 4 | Bathymetric signatures of unfaulting in the Atlantic Ocean. Left: Bathymetric cross sections with fault scarps highlighted in color. Right: Plots of cumulative fault heave vs. distance at selected sections of the Mid-Atlantic Ridge. Corresponding values of T, T', and x_c are listed in Supplementary Table 3.

Extended Data Figure 5 | Bathymetric signatures of unfaulting in the Indian Ocean. Left: Bathymetric cross sections with fault scarps highlighted in color. Right: Plots of cumulative fault heave vs. distance at selected sections of the Southwest Indian Ridge (SWIR) and Carlsberg Ridge. Corresponding values of T, T', and x_c are listed in Supplementary Table 3.

Extended Data Figure 6 | Unfaulting along the intermediate-spreading Chile Ridge. (a) Bathymetric map of the Chile Ridge axis outlining its major segments, adapted from ref. 24. Insets detail bathymetry of segments N1 and N9N–N9S. **(b)** Position and **(c)** amplitude of the change in apparent T at the Chile Ridge: histograms of x_c and (T-T') for all transects across the Chile Ridge, excluding poor fits highlighted in gray in Supplementary Table 3. **(d)** Average slope of axis-facing scarps vs. distance to the ridge axis. Data are from the fault scarp compilation of ref. 24.

Extended Data Figure 7 | Tectonically-accommodated strain along the Chile Ridge. Cumulative fault heave vs. distance from the axis along individual transects from each segment of the Chile Ridge, based on the fault scarp compilation of ref. 24. Red and yellow dots correspond to the western and eastern side of the axis, respectively, with best-fitting piece-wise linear functions shown as black lines. This excludes poor fits highlighted in gray in Supplementary Table 3.

Extended Data Figure 8 | Amplitude and position of the change in apparent *T* along the Chile Ridge. **(a–i)** Histograms of the amplitude of the change (T-T') in apparent T in each bathymetric transect, grouped by segment. **(j–r)** Histograms of the distance x_c where the change in apparent T occurs in each bathymetric transect. These plots exclude poor fits highlighted in gray in Supplementary Table 3.

Extended Data Figure 9 | Lack of unfaulting near an axial high. **(a)** Bathymetric map of the fast-spreading East Pacific Rise at 9°30'N, which unlike every other ridge section studied here features an axial high instead of an axial valley. White line indicates location of bathymetric transect. **(b)** Bathymetric cross sections with fault scarps highlighted in color. **(c)** Cumulative fault heave vs. distance, with best-fitting piece-wise linear function shown as black lines. In this case T' > T.

Extended Data Figure 10 | Mechanics of ridge shoulder unbending. The lithosphere's yield stress σ_y is defined as the difference between the vertical and horizontal stresses needed to produce fault slip. (**a**) shows an idealized plate that was accreted with curvature and no bending stresses. σ_0 is an assumed background stress difference. The simple case shown has no cohesion and parameters A and B depend strongly on the friction coefficient f and assumed pore pressure P_P on the faults, as defined in the Supplementary Information text. (**b**) shows a case with reverse faults that are three times stronger than normal faults, while (**c**) illustrates deepening of the neutral depth, D, when the reverse faults are assumed to be weaker than the normal faults. **(d)** Analytical estimate of the neutral depth D, which marks the base of the compressive zone in an unbending ridge shoulder. The ratio of D to the layer thickness, H, is plotted versus the ratio of pore pressures on reverse versus normal faults assuming f = 0.75 and that the pore pressure on normal faults is 1/3 the lithostatic pressure (Blue curve). Assuming a rock density of 3000 kg/m^3 and water density of 1000 kg/m^3, the left limit is for hydrostatic pore pressure on the reverse faults while the right limit is for lithostatic pore pressure on the reverse faults. Red curve shows the effect on the neutral depth of a regional horizontal extensional stress difference equal to 20% of the extensional yield stress at the base of the layer. See Supplementary Information text for details.

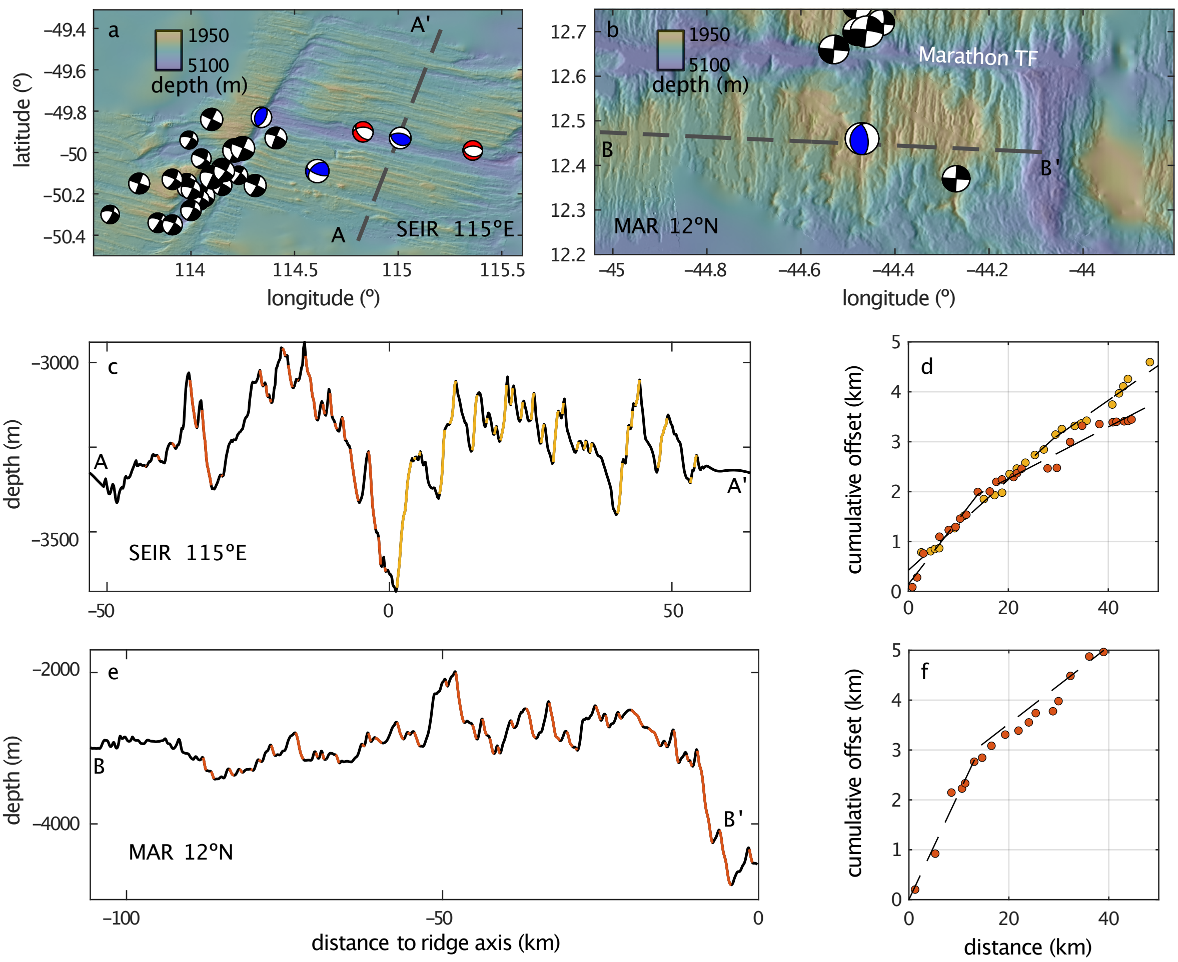

a
1950
5100
depth (m)
A'
A
SEIR 115°E
latitude (º)
longitude (º)
b
1950
5100
depth (m)
Marathon TF
B
B'
MAR 12°N
longitude (º)
c
A
A'
SEIR 115°E
depth (m)
d
cumulative offset (km)
e
B
B'
MAR 12°N
depth (m)
distance to ridge axis (km)
f
cumulative offset (km)
distance (km)

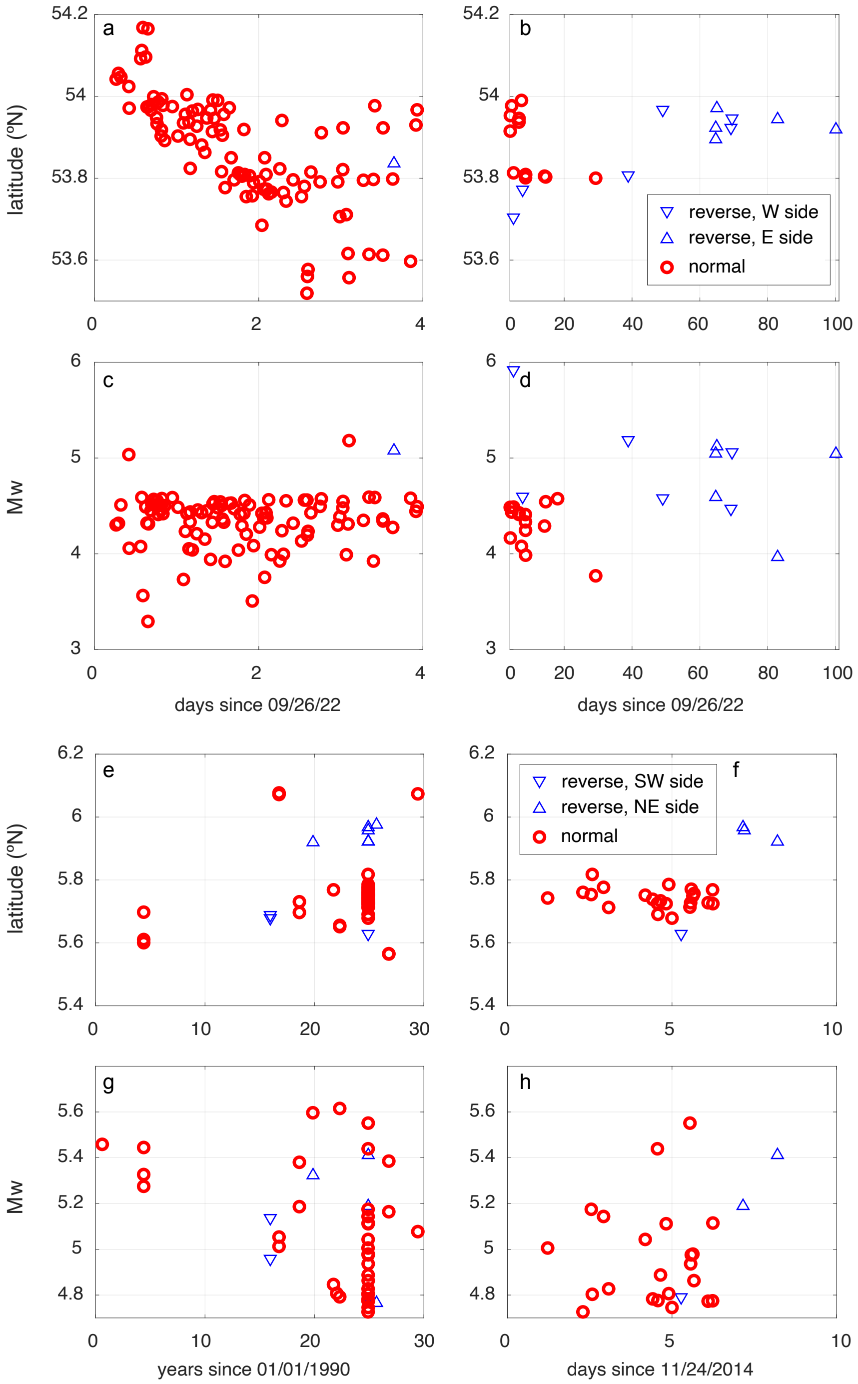

a
b
c
d
e
f
g
h
latitude (ºN)
Mw
days since 09/26/22
years since 01/01/1990
days since 11/24/2014
reverse, W side
reverse, E side
normal
reverse, SW side
reverse, NE side
normal

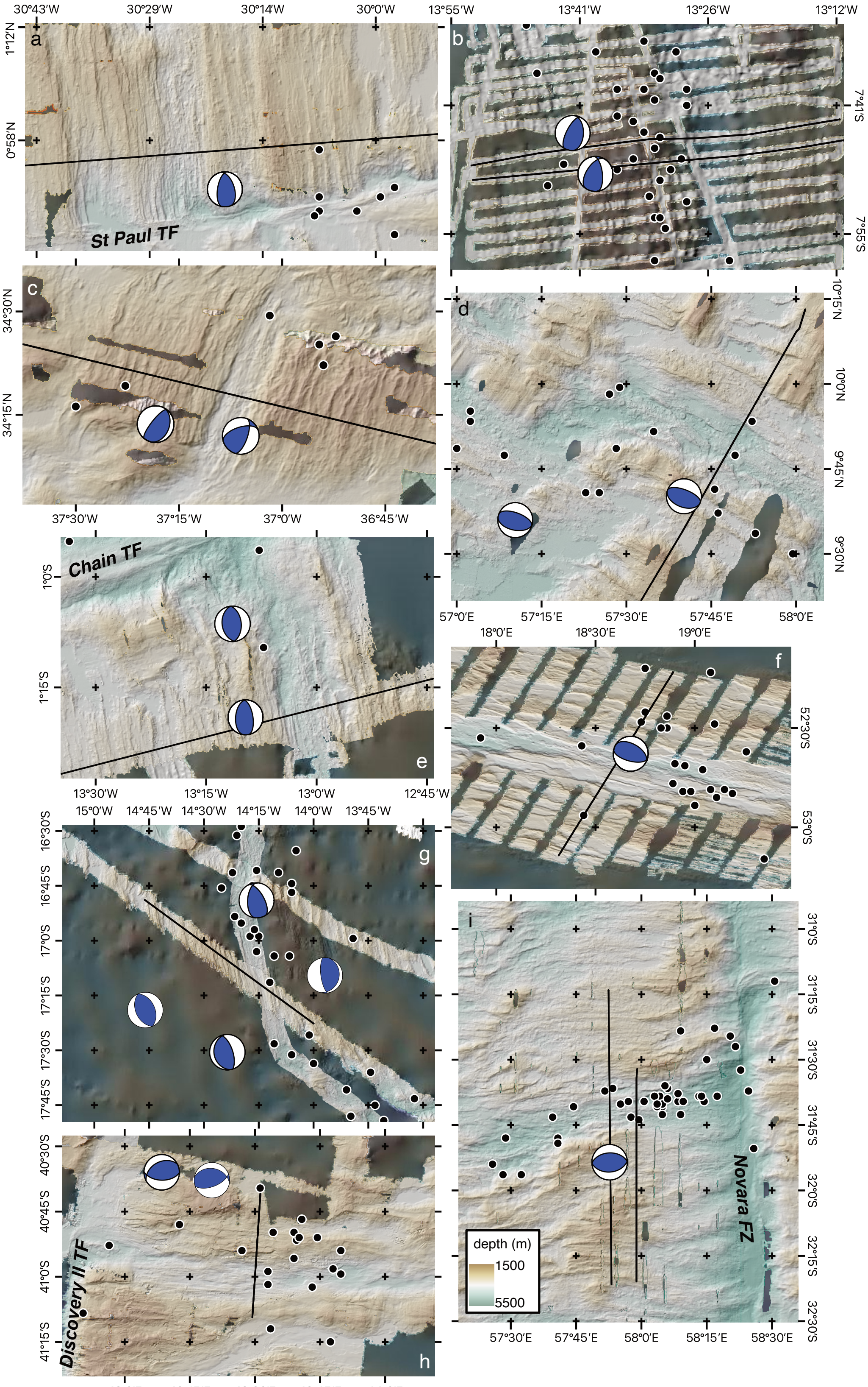

a
St Paul TF
30°43′W
30°29′W
30°14′W
30°0′W
1°12′N
0°58′N
b
13°55′W
13°41′W
13°26′W
13°12′W
7°41′S
7°55′S
c
34°30′N
34°15′N
37°30′W
37°15′W
37°0′W
36°45′W
d
10°15′N
10°0′N
9°45′N
9°30′N
57°0′E
57°15′E
57°30′E
57°45′E
58°0′E
e
Chain TF
1°0′S
1°15′S
13°30′W
13°15′W
13°0′W
12°45′W
f
18°0′E
18°30′E
19°0′E
52°30′S
53°0′S
g
15°0′W
14°45′W
14°30′W
14°15′W
14°0′W
13°45′W
16°30′S
16°45′S
17°0′S
17°15′S
17°30′S
17°45′S
h
Discovery II TF
40°30′S
40°45′S
41°0′S
41°15′S
43°0′E
43°15′E
43°30′E
43°45′E
44°0′E
i
Novara FZ
31°0′S
31°15′S
31°30′S
31°45′S
32°0′S
32°15′S
32°30′S
57°30′E
57°45′E
58°0′E
58°15′E
58°30′E
depth (m)
1500
5500

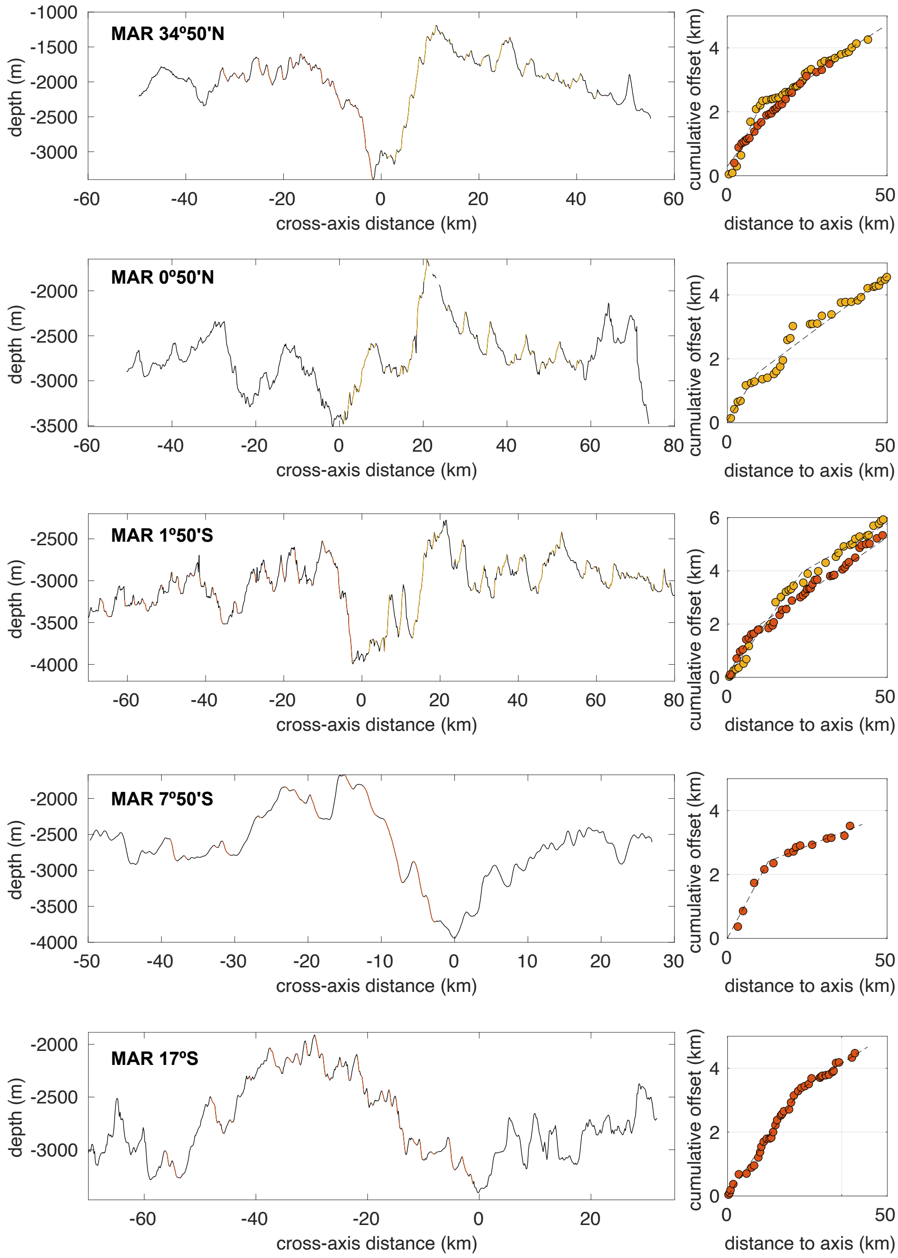

MAR 34º50'N
depth (m)
cross-axis distance (km)
cumulative offset (km)
distance to axis (km)
MAR 0º50'N
MAR 1º50'S
MAR 7º50'S
MAR 17ºS

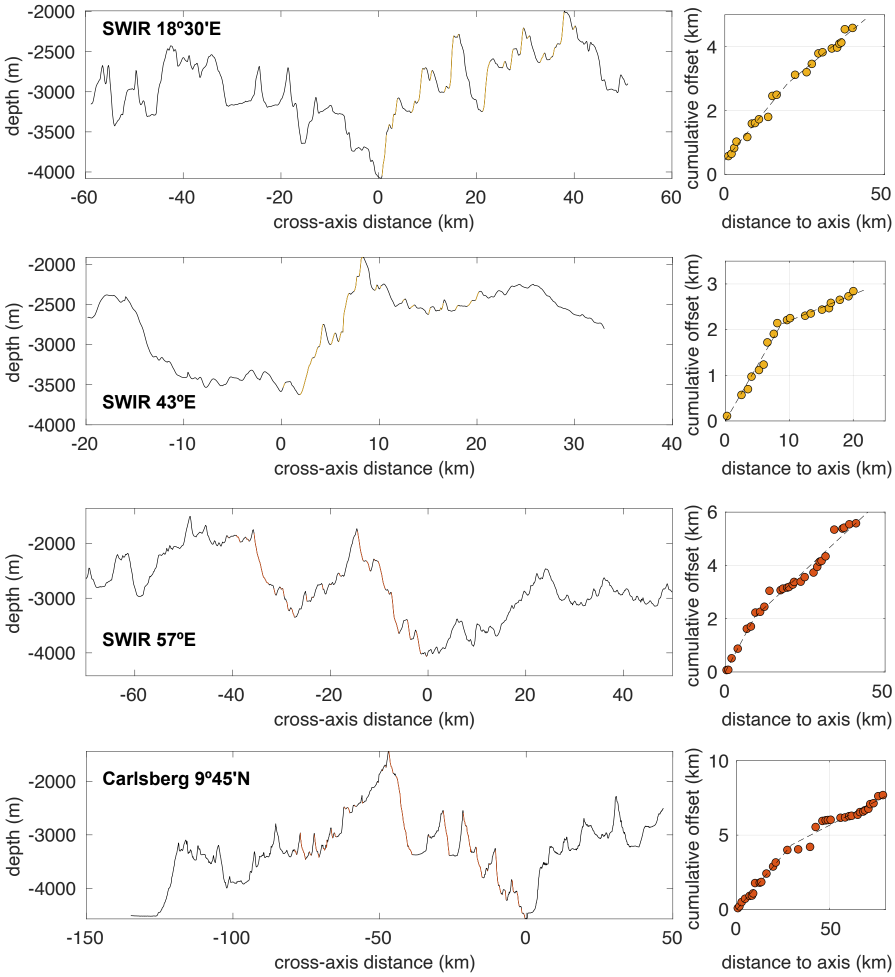
SWIR 18º30'E
SWIR 43ºE
SWIR 57ºE
Carlsberg 9º45'N
depth (m)
cross-axis distance (km)
cumulative offset (km)
distance to axis (km)

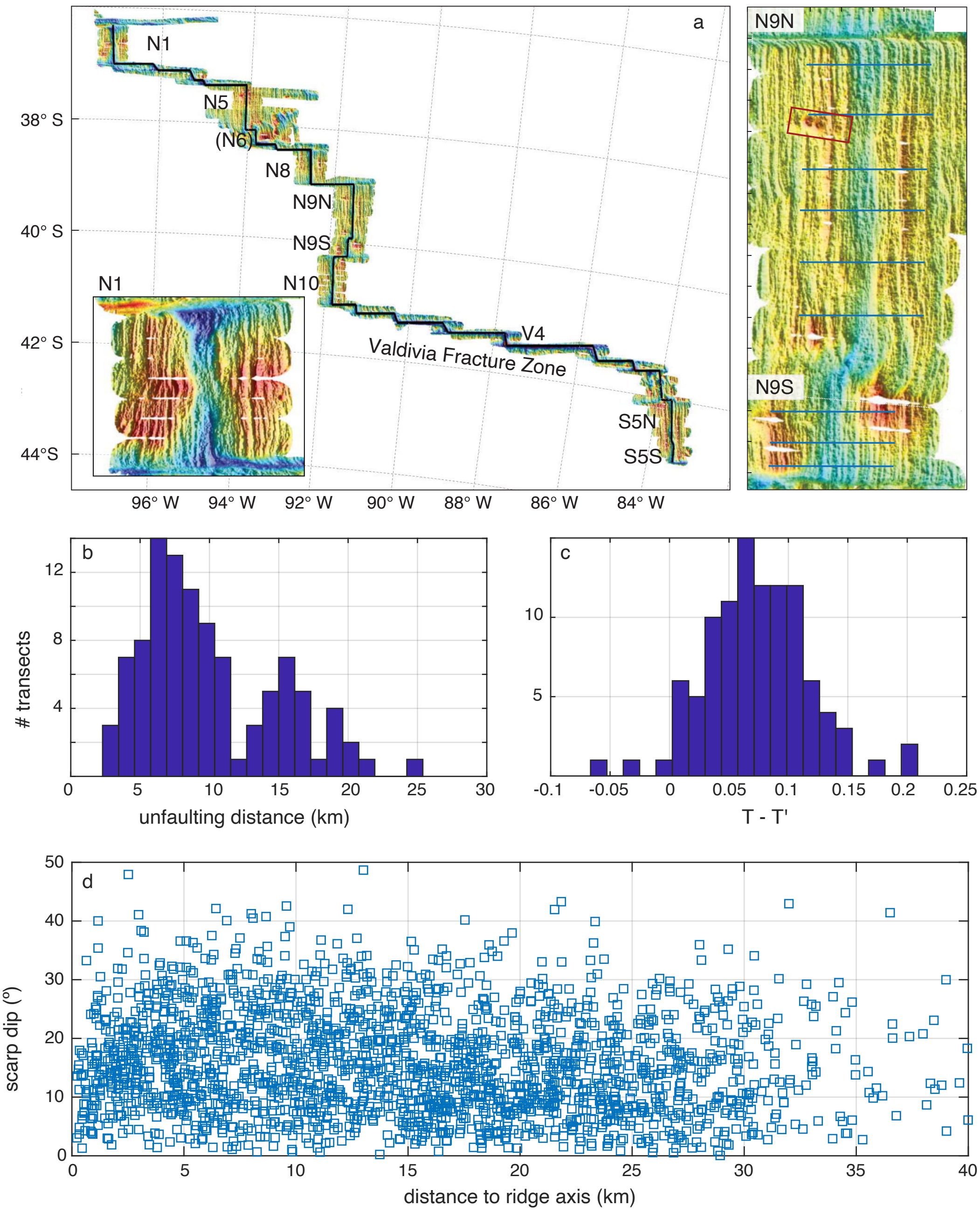

a
N1
N5
(N6)
N8
N9N
N9S
N10
V4
Valdivia Fracture Zone
S5N
S5S
38° S
40° S
42° S
44°S
96° W
94° W
92° W
90° W
88° W
86° W
84° W
N1
N9N
N9S
b
transects
unfaulting distance (km)
c
T - T'
d
scarp dip (°)
distance to ridge axis (km)

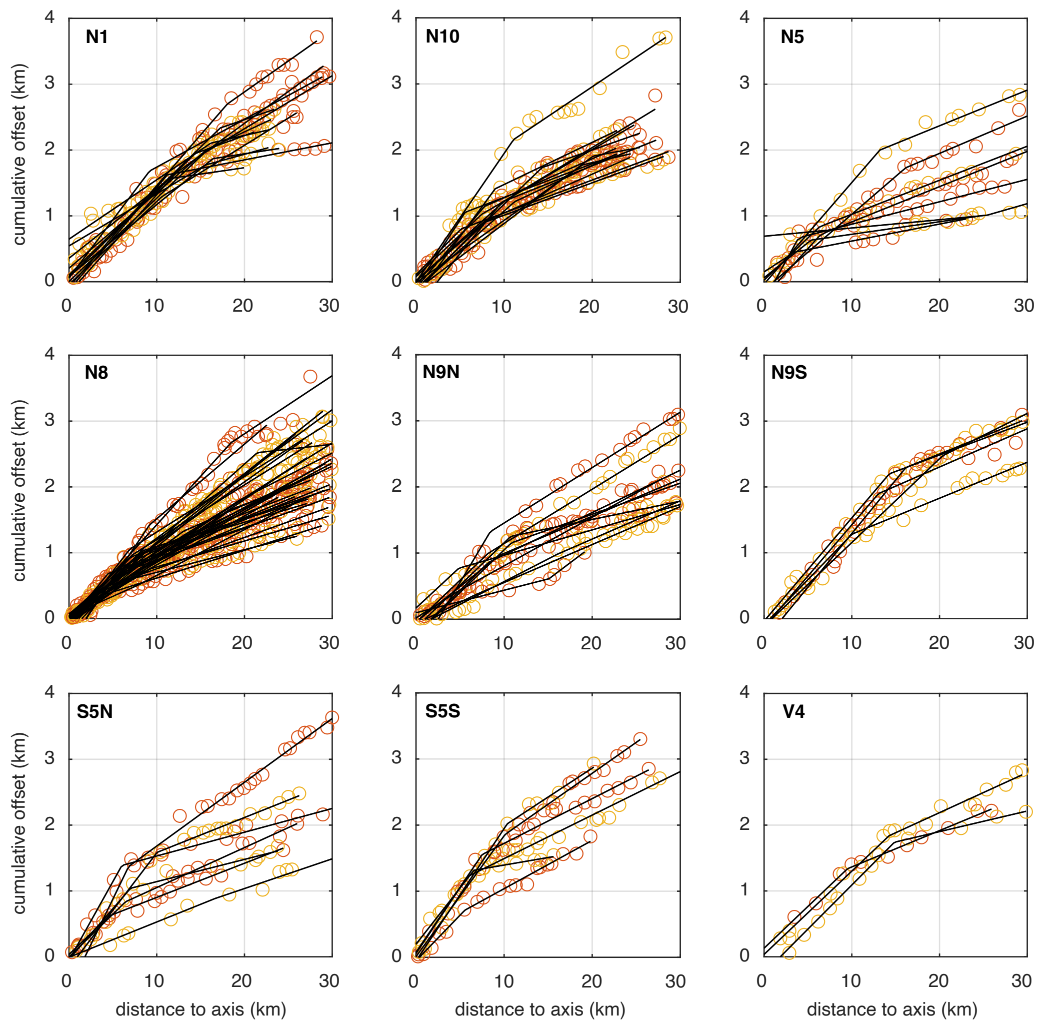

N1
N10
N5
N8
N9N
N9S
S5N
S5S
V4
cumulative offset (km)
distance to axis (km)
0
1
2
3
4
0
10
20
30

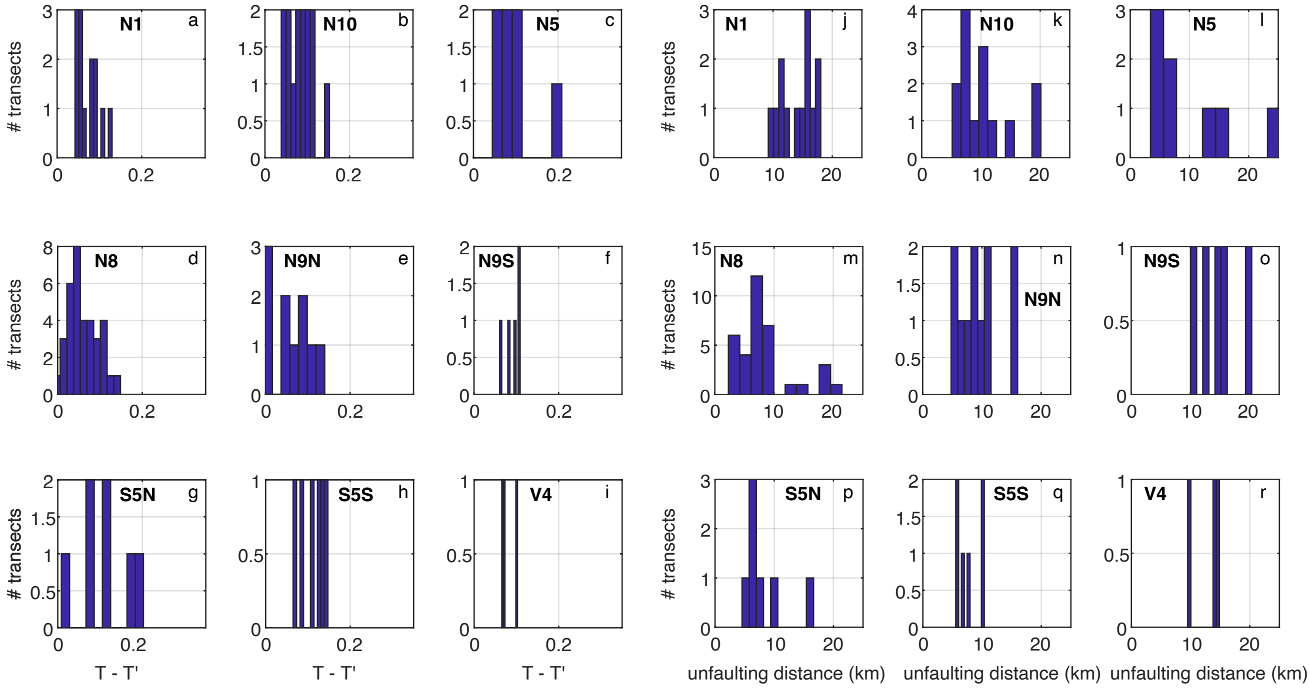
N1
a
N10
b
N5
c
N1
j
N10
k
N5
l
N8
d
N9N
e
N9S
f
N8
m
N9N
n
N9S
o
S5N
g
S5S
h
V4
i
S5N
p
S5S
q
V4
r
transects
T - T'
unfaulting distance (km)

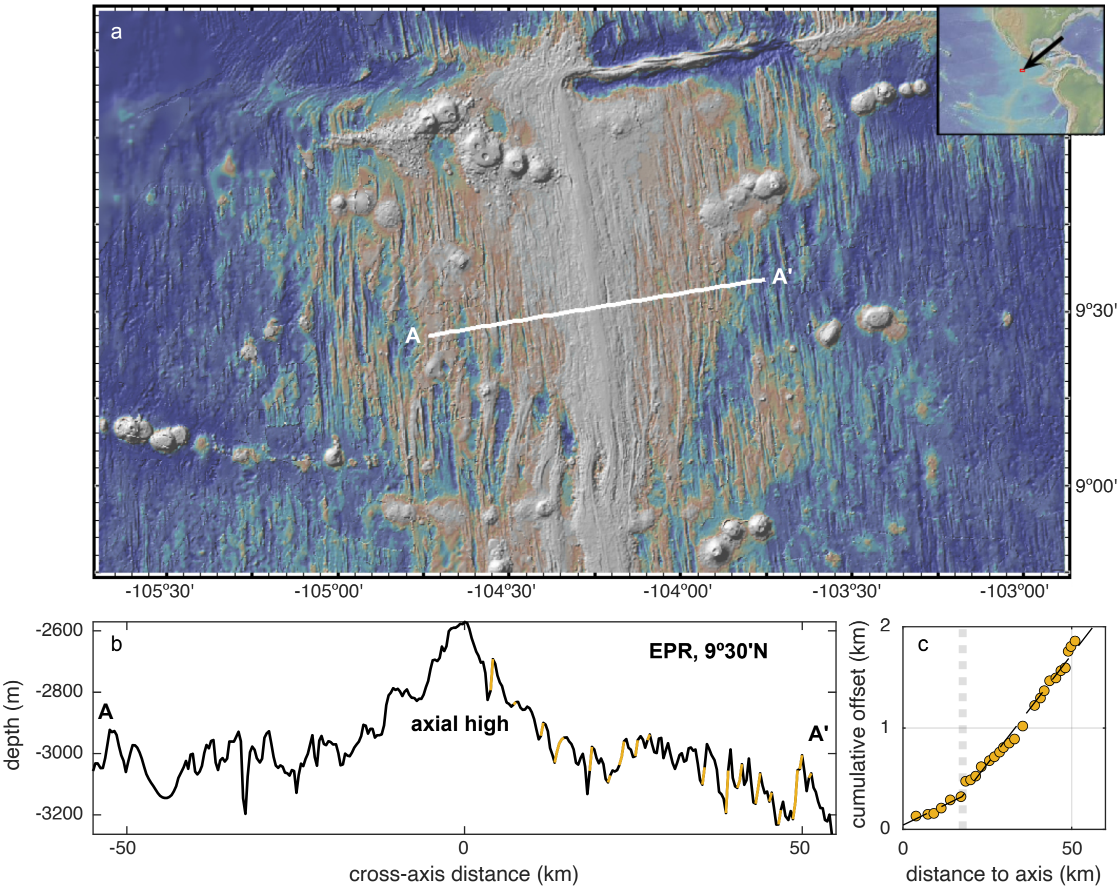

a
A
A'
9°30'
9°00'
-105°30'
-105°00'
-104°30'
-104°00'
-103°30'
-103°00'
b
EPR, 9°30'N
axial high
depth (m)
-2600
-2800
-3000
-3200
-50
0
50
cross-axis distance (km)
c
cumulative offset (km)
2
1
0
distance to axis (km)

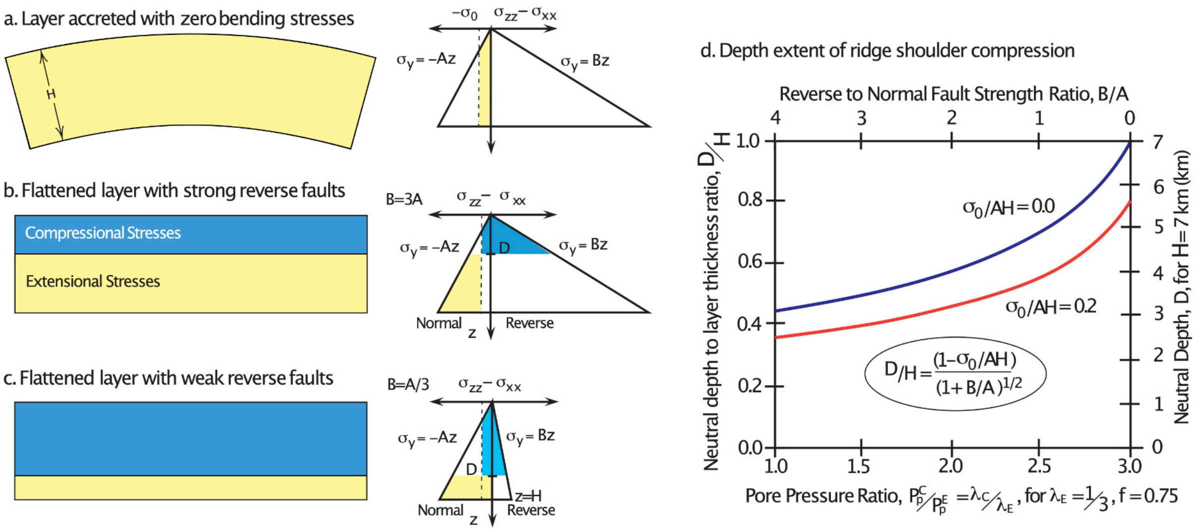

a. Layer accreted with zero bending stresses
H
$-\sigma_0$
$\sigma_{zz}-\sigma_{xx}$
$\sigma_y=-Az$
$\sigma_y=Bz$
b. Flattened layer with strong reverse faults
Compressional Stresses
Extensional Stresses
B=3A
D
Normal
Reverse
z
c. Flattened layer with weak reverse faults
B=A/3
z=H
d. Depth extent of ridge shoulder compression
Reverse to Normal Fault Strength Ratio, B/A
Neutral depth to layer thickness ratio, D/H
Neutral Depth, D, for H=7 km (km)
$\sigma_0/AH=0.0$
$\sigma_0/AH=0.2$
$D/H=\frac{(1-\sigma_0/AH)}{(1+B/A)^{1/2}}$
Pore Pressure Ratio, $P_p^C/P_p^E=\lambda_C/\lambda_E$, for $\lambda_E=1/3$, f=0.75

Supplementary Information for "Mid-ocean ridge unfaulting revealed by magmatic intrusions"

Jean-Arthur Olive[1], Göran Ekström[2], W. Roger Buck[2], Zhonglan Liu[3], Javier Escartín[1] and Manon Bickert[4]

1 - Laboratoire de Géologie, CNRS - École normale supérieure - PSL University, Paris, France
2 - Lamont-Doherty Earth Observatory, Columbia University, Palisades, NY 10964, USA
3 - College of Earth Sciences, Jilin University, Changchun 130061, China
4 - Geo-Ocean, Univ Brest, CNRS, Ifremer, UMR6538, F-29280 Plouzané, France

Content

This supplementary file contains:

• A description of Supplementary Tables 1–4.

• An extended Methods section describing the fault scarp dataset from the Chile Ridge, and detailing a simple analytical model for the depth of the compressive zone taking into account the effect of pore fluid pressure.

Description of supplementary tables

Supplementary Table 1 | Relocated earthquakes at the Mid-Atlantic and Carlsberg Ridge. Event code follows convention of GCMT Catalog. Table also includes depth estimates for 4 events from the 2022 MAR 53ºN earthquake swarm.

Supplementary Table 2 | Unfaulting earthquakes. List of reverse earthquakes from the GCMT catalog that occurred in areas mapped with high-resolution shipboard echo-sounders. Events labeled JM_X are part of the compilation from Jackson & McKenzie (2023).

Supplementary Table 3 | Compilation of unfaulting signatures in high-resolution seafloor bathymetry. Best-fitting slope T of cumulative fault offset vs. distance to the ridge axis near the axis (T best, with maximum and minimum estimates), and away from the axis (T'), past critical distance x_c. Each row is a bathymetric transect on a specified side of the ridge axis. Shaded rows are transect that did not yield a satisfactory fit with a piece-wise linear function.

Supplementary Table 4 | Normal faults along the Chile Ridge. Original dataset from Howell et al. (2016). Each fault is identified along a ridge-normal transect by the position of the bottom and top of its seafloor scarp (locations 1 and 2). Positive and negative distance to the ridge axis correspond to fault located west and east of the axis, respectively. Segments are numbered as follows (#1–#9): N1, N10, N5, N8, N9N, N9S, S5N, S5S, and V4.

Supplementary Methods

Bathymetric evidence of unfaulting without seismic manifestation: the Chile Ridge

A dataset of fault scarps previously identified along the entire Chile Ridge by Howell et al. (2016) (Supplementary Table 4) was also used to construct Extended Data Figs. 6–8. In Fig. 2, faults from both sides of the ridge are fitted together, while in Extended Data Figs. 1, 4, 5, 7, faults from each side of the ridge are fitted separately. We find that this choice has little influence on the results, which are summarized in Supplementary Table 3. At 12 transects out of 114 at the Chile Ridge, the non-linear least-squares method yielded unrealistically wide bounds on T and x_c. We interpret these as indicative of a non-robust fit (highlighted in gray in Supplementary Table 3), and exclude the corresponding transects from the plots shown in Extended Data Figs. 6–8. Overall, the mean unfaulting strain across the Chile Ridge is 0.074 (±0.044 of standard deviation, Extended Data Fig. 6), and this value is representative of all segments (Extended Data Fig. 8a–i). The unfaulting distance displays a bimodal distribution, with peaks at ~7 and ~16 km (Extended Data Fig. 6b). This distribution reflects segments with a short unfaulting distance (~5–10 km), such as N8, N9N, S5S and S5N, and segments with x_c between 10 and 20 km, such as N1, N9S, and V4. Segments N10 and N5 show a wider range in x_c (Extended Data Fig. 8j–r).

Extended Data Fig. 6d further shows no distinct change in the slopes of axis-facing (abyssal hill bounding) fault scarps as they migrate off axis past the unfaulting distance. This suggests that the change in apparent T fraction identified in our fault strain plots is unlikely due to slope-reworking mass wasting processes, and instead have a tectonic origin that affects fault offset rather than scarp slope.

An analytical model for ridge flank compression modulated by pore fluid pressures

Analytical and numerical models suggest that the flattening of axial bathymetric relief occurs via lithospheric un-bending (e.g. Buck, 2001; Liu and Buck, 2018). The prefix "un-" is used because analysis suggests that lithosphere at spreading centers accretes in a "bent" state (i.e., with curvature "built in"). For ridges with an axial high (Extended Data Fig. 9), as at most fast-spreading centers, the initial curvature is concave up. For ridges with an axial valley, as at most slow-spreading centers, this curvature is concave down. The un-bending flanking an axial valley puts the top of the plate in compression and the base of the plate in extension.

Many tectonic models make a simplifying assumption that normal and reverse faults are subject to hydrostatic pore pressures (e.g., Brace and Kohlstedt, 1980). Models of axial valley formation that make this standard assumption predict a very shallow depth extent of reverse faulting during unbending (e.g., ~2 km in Fig. 3). This may be a problem, in terms of explaining the observations discussed in this paper, for two reasons. First, it is hard to reconcile the large magnitude of the 2022 reverse faulting earthquakes on the MAR, up to magnitude 5.9, with a small depth extent of reverse fault slip. The moment magnitude should scale with fault area and fault slip. The fault area depends on the depth extent and axis-parallel extent of fault slip. Though bending faults appear to be longer than faults that cut a brittle layer (e.g., Supak et al., 2006) it is likely that such large magnitude earthquakes must happen on faults that cut more deeply than ~2 km. This is especially true since slip on bending faults should linearly decrease with distance from the top of the strong lithospheric plate and vanish at the "neutral depth" of bending (inset in Fig. 4a). The second problem with the assumption of hydrostatic pore pressures on reverse faults is that it results in a wide zone of un-bending strain with distance from the spreading axis. In the model of Fig. 3, the zone of unbending is ~30 km wide. This implies a wide zone of slip on reverse faults, and that would result in a similarly wide zone of reduction in abyssal hill relief. This is counter to the observed <10 km wide zone of reduction in abyssal hill relief as shown in Fig. 2, as well as most T-fraction vs. distance plots shown in this study.

One possible explanation for these observations is that reverse faults flanking axial valleys are subject to the same high levels of pore pressures apparently affecting reverse faults in convergent settings. The idea of such high pore pressures on reverse faults comes from consideration of seismic reflection observations in some mountain ranges showing thrusting of several hundred-kilometer-wide packages of crustal rocks on almost flat reverse faults, or décollements (e.g., Bally et al., 1966). Hubbert and Rubey (1959) showed that these décollements had to be far weaker than expected to allow such large-scale thrusting. Those authors proposed that high pore water pressure, approaching lithostatic levels, was the likely mechanism allowing reverse slip at very low shear stress. Near-lithostatic pore pressure is also the accepted explanation for the shapes of many accretionary prisms above subducting plates (e.g., Davis et al., 1983). The fact that normal faults are not known to be associated with higher-than-hydrostatic pore pressures (e.g., Axen and Selverstone, 1994) makes mechanical sense because pore pressures greater than the minimum compressive stress should result in fracturing that relieves those high pore pressures.

High pore pressures on reverse faults should make those faults effectively weaker in that they would slip at lower levels of shear stress. Weakening reverse faults relative to normal faults should allow them to slip down to greater depths, as bending should not change the average horizontal stress in a layer. This is because flexure should not affect the horizontal force balance of a floating layer. Un-bending of an initially concave down layer, as shown in Extended Data Fig. 10, puts the top of the layer in compression and the bottom of the layer in extension, but the average stress change should be zero. More precisely, the integral of bending-induced horizontal stresses with respect to depth has to equal zero (e.g., Bodine et al., 1981). Compressional fault slip should occur down to the depth where the bending stress is zero, which is termed the neutral depth, D. Below, we estimate the effect of reverse fault weakening on the neutral depth of bending, using the thin plate flexure approximations (e.g., Watts, 2002).

Thin plate theory relates bending of a layer that is thin compared to the horizontal scale of bending. If h is the elevation of the plate surface relative to some datum then the plate has a curvature of ${dh^2}/{dx^2}$ where x is the horizontal distance from the axis in the direction of spreading. An approximate scaling gives the initial curvature of the plate at $x = 0$ as ${2h_0}/{w^2}$ where h_0 is the depth of the axial valley relative to the flanks and w is the half-width of the valley (Buck, 2001). If the plate is flattened out then the change in curvature is about ${2h_0}/{w^2}$. Thin plate theory holds that the horizontal strain, ε_{xx}, in a layer experiencing a change in curvature, $\Delta\, {dh^2}/{dx^2}$, varies with vertical distance, z', from the depth in the plate where the bending strain is zero (the neutral depth D) as:

$$\varepsilon_{xx}(x, z) \cong z'\Delta\, {dh^2}/{dx^2} \cong (D - z)\, {2e_0}/{w^2}\,, \qquad (1)$$

where z is depth below the surface.

We first consider the case of a plate of thickness h with uniform elastic properties and show that the bending stresses should be so large that parts of the plate would yield by faulting. The horizontal stress produced by bending is:

$$\sigma_{xx}(x, z) = \frac{E}{(1-\nu^2)}\, \varepsilon_{xx}(z) \qquad (2)$$

where E is Young's Modulus and ν is Poisson's Ratio for the lithosphere. For unbending of axial valley lithosphere of thickness H the maximum compressional stress is at the top of the lithosphere where for uniform properties $z' = {H}/{2}$. Taking lithospheric thickness $H = 5\ km$, valley depth $e_0 = 1000\ m$, $w = 15\ km$ and assuming reasonable values for rock elastic constants of $E = 5\text{x}10^{10}$ Pa and $\nu = 0.25$ gives a maximum compressive stress of $\sim 10^{10}$ Pa. This is more than 2 orders of magnitude greater than the yield stress for faulting at several kilometers depth, as we will show below. For such elastic bending stress the top of the plate (i.e., shallower than D) is at the yield stress for reverse faulting and below z_N the plate is at extensional yield. In previous work on lithospheric bending the inclusion of brittle yielding decreases the effective horizontal length scale of yielding (e.g., Bodine et al., 1981; Buck, 1988). This effect may help explain the narrow zone of unbending that we infer from the observed patterns of cumulative fault offset with distance from a spreading center.

We follow many workers in defining the brittle yield stress in terms of the stress difference needed to slip on an ideally oriented fault in an Andersonian stress field (e.g., Brace and Kohlstedt, 1980). An Andersonian stress field is one in which the principal stresses are either parallel to or normal to the surface of the lithosphere (Anderson, 1951). Here we use the engineering convention that tension is positive. For compressional faulting the maximum principal stress is vertical (i.e., σ_{zz}) while for extensional faulting the maximum principal stress is horizontal (i.e., σ_{xx}). The ideal fault orientation is taken to give the minimum stress difference for slip on a fault with a friction coefficient *f*. A detailed derivation of the stress needed for slip (or yielding) on ideally-oriented faults is given in Turcotte and Schubert (2002). It is common to represent the pore pressure as $P_p = \lambda\rho g z$, where λ is the ratio of pore pressure to vertical stress ($\sigma_{zz} = \rho g z$), ρ is the density of the lithosphere and g is the acceleration of gravity. Then, the brittle yield stress (a stress difference) for normal (extensional) faulting, writes:

$$\sigma_Y^E(z) = \sigma_{zz} - \sigma_{xx} = \frac{-2f(1-\lambda_E)\rho g z}{(1+f^2)^{\frac{1}{2}}+f} = -Az$$

and for reverse (compressional) faulting, assuming $P_p = \lambda_C \rho g z$, is: (3)

$$\sigma_Y^C(z) = \sigma_{zz} - \sigma_{xx} = \frac{2f(1-\lambda_C)\rho g z}{(1+f^2)^{\frac{1}{2}}-f} = Bz$$

This implies that at any depth the ratio of the magnitude of the yield stresses is:

$$\left|\frac{\sigma_Y^C(z)}{\sigma_Y^E(z)}\right| = \frac{B}{A} = \frac{(1-\lambda_C)\left[(1+f^2)^{\frac{1}{2}}+f\right]}{(1-\lambda_E)\left[(1+f^2)^{\frac{1}{2}}-f\right]} \tag{4}$$

The neutral depth is the depth that makes the integral of the bending stresses zero. This can be seen graphically in Extended Data Fig. 10 as requiring the area in blue to match the area in yellow on the yield stress plots. Since there is normal faulting within an axial valley, we expect that the average horizontal stress is non-zero and is extensional. Assuming that the average stress difference is $-\sigma_0$ the neutral depth for strong un-bending resulting in zero net bending stress is:

$$\frac{D}{H} = \frac{\left(1-{\sigma_0}/{Ah}\right)}{\sqrt{1+{B}/{A}}} \tag{5}$$

Extended Data Fig. 10 shows that the neutral depth is strongly dependent on the ratio of compressional to extensional frictional yield stress (i.e., *B*/*A*) and on the background stress difference σ_0. It also shows how D varies with the pore pressure on reverse faults (panel d). For example, if the friction coefficient $f = 0.75$ and the same pore pressure acts on normal and reverse faults then *B*/*A*=4. Assuming a rock density of 3000 kg/m^3, hydrostatic pore pressure on a normal fault implies that $\lambda_E = {\rho_w}/{\rho} \approx {1000}/{3000}$ so that for $f = 0.75, A \approx (1/2)\rho g z$. To have *B*/*A*=1 then would require that $\lambda_C = 0.83$. This appears reasonable as larger pore pressure ratios have been estimated for convergent setting (e.g., Davis et al., 1983).

Other factors are likely to affect the depth range of unbending-related reverse faulting on the flanks of an axial valley. For example, inclusion of viscoelastic effects may result in a deepening of the maximum depth of thrusting. We expect this because on the long-time interval between bending earthquakes the lower lithosphere can flow viscously to relax stress differences. On the short time interval of an earthquake the lower lithosphere should maintain large stress differences. However, such effects are not simple to quantify since they require a numerical solution with very high spatial and temporal resolution.

References

Anderson, E.M. The Dynamics of Faulting, 206 pp., Oliver and Boyd, Edinburgh (1951)

Axen, G.J. & Selverstone, J. Stress-state and fluid-pressure level along the Whipple detachment fault, California. *Geology* **22**, 835–838 (1994)

Bally, A.W., Gordy, P.L. & Stewart, G.A. Structure, seismic data, and orogenic evolution of the southern Canadian Rockies. *Bull. Can. Pet. Geol.* **14**, 337–381 (1966)

Bodine, J. H., Steckler, M.S. & Watts, A.B. Observations of flexure and the rheology of the oceanic lithosphere. *J. Geophys. Res.* **86**, 3695–3707 (1981)

Brace, W.F. & Kohlstedt, D.L. Limits on lithospheric stress imposed by laboratory experiments. *J. Geophys. Res.* **85**, 6248-6252 (1980)

Buck, W.R. Accretional curvature of lithosphere at magmatic spreading centers and the flexural support of axial highs. *J. Geophys. Res.* **106**, 3953–3960 (2001)

Buck, W.R. Flexural rotation of normal faults, *Tectonics* **7**, 959–974 (1988)

Davis, D., Suppe, J. & Dahlen, F.A. Mechanics of fold-and-thrust belts and accretionary wedges. *J. Geophys. Res.* **88**, 1153–1172 (1983)

Howell, S., Ito, G., Behn, M. D., Martinez, F., Olive, J.-A. & Escartín, J. Magmatic and tectonic extension at the Chile Ridge: Evidence for mantle controls on ridge segmentation, *Geochem. Geophys. Geosyst.*, 17 (2016)

Hubbert, M.K. & Rubey, W.W. Role of fluid pressures in mechanics of overthrust faulting: I. mechanics of fluid-filled porous solids and its application to overthrust faulting. *GSA Bulletin* **70**, 115–166 (1959)

Jackson, J. & McKenzie, D. Reverse-faulting earthquakes and the tectonics of slowly-spreading mid-ocean ridge axes. *Earth Planet. Sci. Lett.* **618** (2023)

Liu, Z. & Buck, W.R. Magmatic controls on axial relief and faulting at mid-ocean ridges. *Earth Planet. Sci. Lett.* **491**, 226-237 (2018)

Supak, S.K., Bohnenstiehl, D.R. &. Buck, W.R. Flexing is not stretching: An analog study of bending induced cracking. *Earth Planet. Sci. Lett.* **246**, 125–137 (2006)

Turcotte, D. L & Schubert, G. Geodynamics, 2nd edition, *Cambridge University Press* (2002)

Watts, A.B. Isostasy and Flexure of the Lithosphere, Cambridge University Press, ISBN: 0-521-622727 (2001)